Organic petrography and pore structure characterization of low-mature and gas-mature marine organic-rich mudstones: Insights into porosity controls in gas shale systems

Amélie Cavelan, Mohammed Boussafir, Olivier Rozenbaum, Fatima Laggoun-Défarge

Accepted Manuscript

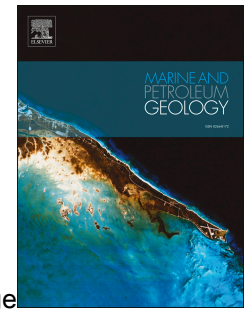

Organic petrography and pore structure characterization of low-mature and gas-mature marine organic-rich mudstones: Insights into porosity controls in gas shale systems

Amélie Cavelan, Mohammed Boussafir, Olivier Rozenbaum, Fatima Laggoun-Défarge

PII: S0264-8172(19)30090-X

DOI: https://doi.org/10.1016/j.marpetgeo.2019.02.027

Reference: JMPG 3741

To appear in: *Marine and Petroleum Geology*

Received Date: 2 November 2018

Revised Date: 27 February 2019

Accepted Date: 28 February 2019

Please cite this article as: Cavelan, Amé., Boussafir, M., Rozenbaum, O., Laggoun-Défarge, F., Organic petrography and pore structure characterization of low-mature and gas-mature marine organic-rich mudstones: Insights into porosity controls in gas shale systems, *Marine and Petroleum Geology* (2019), doi: https://doi.org/10.1016/j.marpetgeo.2019.02.027.

Organic petrography and pore structure characterization of low-mature and gas-mature marine organic-rich mudstones: insights into porosity controls in gas shale systems.

Amélie Cavelan[a,b,c*], Mohammed Boussafir[a,b,c], Olivier Rozenbaum[d], Fatima Laggoun-Défarge[a,b,c]

(a) Université d'Orléans, ISTO, UMR 7327, 45071 Orléans, France

(b) CNRS, ISTO, UMR 7327, 45071 Orléans, France

(c) BRGM, ISTO, UMR 7327, BP 36009, 45060 Orléans, France

(d) CNRS, CEMHTI, UPR 3079, 45071 Orléans, France

*Corresponding author, Email: amelie.cavelan@cnrs-orleans.fr

Abstract- Analyses of both type II organic-rich low-mature mudstones from the Kimmeridge Clay Formation (Yorkshire, England) and gas-mature mudstones from the Vaca Muerta formation (Argentina) were performed using petrographic and SEM observations to characterize the organic and inorganic components of the rocks and their relationship with porosity. The porosity analyses using nitrogen adsorption measurements and mercury intrusion porosimetry were then evaluated as a function of both composition and thermal maturity. Despite the absence of variation in the pore size distribution and the total pore volume with maturity, which is controlled by total organic carbon content (TOC), this study demonstrates that the pore network of these marine mudstones varies considerably with thermal maturity. Contrary to low-mature samples, whose porosity depends essentially on mineral interparticle pores, the porosity of thermally-mature rocks is mainly influenced by organic-matter-hosted pores located within secondary solid bitumen. Organic matter (OM) porosity, which is rare in the low-mature stage, appears to increase during thermal maturation in response to the thermal cracking of kerogen and oil, to become predominant in gas-mature rocks. It can therefore be considered that thermal maturation is a major process for the development of the OM porosity. However, the OM of high-TOC (>5.5 wt.%) gas-mature samples contains smaller pores than gas-mature low-TOC mudstones probably due to a difference in the original OM composition between

these high- and low-TOC samples. By analogy with the Kimmeridge Clay formation, which is often considered as time equivalent in terms of OM composition (Uliana et al., 1999), the high-TOC Vaca Muerta samples appear to have originally contained greater proportions of oil-prone amorphous OM and thus a better OM intrinsic quality for oil generation. This difference of OM composition and petroleum potential between Vaca Muerta marine mudstones appears to have dramatically influenced the OM-hosted pore genesis during maturation. Consistent with other studies, these results show that thermal maturity is not the only process that can explain OM-hosted pore genesis in gas shale systems. The OM composition can greatly influence the evolution of this porosity during maturation. Organic composition and OM thermal maturity may therefore have a complementary effect, explaining the diversity of trends observed on porosity in natural formations.

Keywords: shales porosity, thermal maturity, organic matter, organic petrography.

1. Introduction

Gas shale systems have been studied for many years, but the origin and the evolution of their pore systems remains incompletely understood. The difficulty lies in the characterization of the features of these rocks whose size is on the order of nm to µm (Ross and Bustin, 2009; Chalmers and Bustin, 2008; Chalmers et al., 2012; Loucks et al., 2012). The porosity of these mudstones is generally subdivided into macropores (pore width >50 nm), mesopores (pore width between 2–50 nm) and micropores (pore width < 2 nm, Sing, 1985) and grouped into three pore classes (Loucks et al., 2012), namely: interparticle pores between mineral grains, intraparticle mineral-hosted pores, and intraparticle organic matter (OM) pores. Quantitative assessments of pore volume and pore size distribution provided by SEM imaging (Curtis et al., 2012; Loucks et al., 2012; Fishman et al., 2012; Ko et al., 2018) and gas adsorption techniques (Chalmers et al., 2012; Kuila et al., 2012; Pan et al., 2015; Tian et al., 2015) revealed that OM porosity is a significant component of the pore networks of gas-mature mudstones. A multitude of factors seem to be responsible for OM-hosted pore genesis and stability in mudstones. Organic richness, OM composition, and OM thermal maturity are the most commonly cited mechanisms (Loucks et al., 2012; Curtis et al., 2012; Ko et al., 2016; Katz and

Arango, 2018). However, there remains a lack of a clear understanding of the respective contribution of these factors to the porosity (Katz and Arango, 2018).

In recent years, the effect of thermal maturity has received special attention due to the growing recognition of its involvement in the genesis of OM-hosted pores (Chalmers and Bustin 2008; Curtis et al., 2012; Loucks et al., 2012; Chen and Xiao, 2014; Ko et al., 2016). Previous studies have shown that type II OM is mainly non-porous from the immature stage to the early oil window (Loucks et al., 2009; Bernard et al., 2012; Curtis et al., 2012). However, some pores are commonly observed in mudstones rich in type III OM (Reed, 2017). Most of these OM-hosted pores appear to be inherited from the original structures of cellulose and woody fragments (Reed, 2017). Nevertheless, OM pores are widely observed in shales containing type II OM from the late oil window to the overmature stage (Bernard et al., 2012; Loucks et al., 2012). It is thus commonly assumed that OM-related porosity increases with thermal maturity in response to the thermal cracking of type II kerogen (Bernard et al., 2012; Loucks et al., 2012; Chen and Xiao, 2014; Ko et al., 2016, 2018). With increasing thermal maturity some by-products called solid bitumen can be formed during the thermal cracking of pre-existing bitumen into oil and gas or from the transformation of a pre-existing liquid oil into gas (Tissot and Welte, 1984; Lewan, 1993; Behar et al., 1997; Reed et al., 2014). Solid bitumen is the dominant maceral in thermally-mature mudstones (Hackley and Cardott, 2016; Hackley, 2017). The carbon-rich residue formed from the secondary cracking of liquid oil (so called pyrobitumen) is considered to be the main contributor to the porosity in thermally-mature mudstones (Bernard et al., 2012; Milliken et al., 2013; Hackley and Cardott, 2016; Hackley, 2017). The bubble-like morphology of some OM-pores in gas-mature rocks has been interpreted as evidence that this porosity stems only from the formation of gas bubbles within pyrobitumen formed after the secondary cracking of liquid oil (Bernard et al., 2012; Milliken et al., 2013). This hypothesis remains nevertheless controversial (Reed et al., 2014) and some evidence shows that pores in OM can form earlier, in the oil window (Juliao et al., 2015).

An increase in OM porosity with thermal maturity has not been systematically and clearly observed, suggesting that the relationship between maturity and OM-hosted porosity is not straightforward (Schieber, 2010; Fishman et al., 2012; Curtis et al., 2012; Löhr et al., 2015; Milliken et

al., 2013). Variations as a function of the OM composition and especially the importance of maceral types have been noted in the last few years (Fishman et al., 2012; Loucks et al., 2012; Milliken et al., 2013; Cardott et al., 2015; Ko et al., 2017, 2018). For a given maturity, the OM-hosted porosity can vary greatly between and within rocks of the same formation (Curtis et al., 2012; Loucks et al., 2012; Milliken et al., 2013; Tian et al., 2015). Moreover, in oil-mature and gas-mature mudstones from the Marcellus formation (Ro= 1.0% and 2.1%, Milliken et al., 2013), high-TOC samples (TOC > 5.6 wt.%) exhibit a reduced pore volume due to smaller pores compared to low-TOC samples. Similar trends were observed for higher TOC samples (TOC > 12 wt.%) in the gas window from the Gufeng, the Longtan and the Dalong formations (Ro= 2.34–2.64 %, Pan et al., 2015). These observations suggest that thermal maturity alone is not sufficient to understand the evolution of porosity in mudstones. The OM typology, its state of preservation and the maceral composition may also influence the development of the OM-hosted porosity (Fishman et al., 2012; Mastalerz et al., 2013; Cardott et al., 2015; Ko et al., 2017, 2018). Many differential compaction phenomena influencing the fabric and the texture of rocks are commonly used to explain these observations such as differences in the relative timing of compaction and cementation or variations in TOC and clay mineral contents (Milliken et al., 2013; Pan et al., 2015; Ko et al., 2017). This issue leads us to ask the following questions. What is the importance of the OM composition compared to compaction/cementation phenomena? What is its contribution to the pore systems of gas-mature mudstones?

In order to better understand the different parameters influencing the nature, structure and the distribution of pores in gas-source rocks, this study investigated low-mature and gas-mature source rocks presenting various organic contents from the Kimmeridge Clay Formation (KCF) and the Vaca Muerta Formation (VMF) respectively. These two formations are often considered as equivalent in terms of OM composition and depositional environment (Uliana et al., 1999). This study first documented the overall organic and inorganic composition and thermal maturation of these mudstones to compare their pore structure as a function of OM maturity and mineral composition; then the organic matter composition of both low-mature and gas-mature mudstones was investigated using Rock-Eval, petrographic observations and palynofacies analysis; and finally their pore structure was characterized with high resolution SEM imaging techniques, mercury intrusion porosimetry, and low-

pressure nitrogen adsorption measurements. Based on these results, the relationships between organic geochemistry, mineralogy and porosity were then examined and compared as a function of thermal maturity. In the present study, the terminology 'mudstones' was used according to the recommendations of Lazar et al. (2015) to refer to rocks containing more than fifty percent of mud-size grains (<62.5 µm, clay and silt).

2. Samples and methods

2.1. Geological settings

Twenty-one samples were obtained from drill cores from the Kimmeridge Clay Formation (KCF) and 12 from the Vaca Muerta Formation (VMF) (Tab.1, Figs.1, 2). The VMF is a marine deposit developed in an ancient backarc embayment known as the Neuquén Basin (Argentina, Fig.1) (Legarreta and Uliana, 1991; Uliana et al., 1999; Legarreta and Villar, 2011; Kietzmann et al., 2011, 2014). This formation consists of a succession of black shales, marls and dark calcareous siltstones interbedded with organic-rich mudstones and wackestones developed from the Tithonian to the Early Valanginian during a global eustatic highstand (Fig.2, Legarreta and Uliana, 1991; Kietzmann et al., 2011, 2014). Mineralogy exhibits variations depending on the basin location (Garcia et al., 2013). Generally, quartz (16–63 wt.%) and plagioclase (1–28 wt.%) are the most abundant components (Garcia et al., 2013; Kietzmann et al., 2016). The proportion of carbonates is inversely correlated to the quartz content and fluctuates greatly over the formation (0–51 wt.%, Kietzmann et al., 2016). Higher clay mineral content is generally observed in the southwestern part of the basin, where it does not exceed ~30 wt.% (Garcia et al., 2013; Kietzmann et al., 2016). These mudstones are characterized by high type II OM contents and are marked by variations in the OM composition (Uliana et al., 1999; Kietzmann et al., 2014). The kerogen is mainly composed of marine amorphous OM associated with variable amounts of marine microplankton and terrestrial materials in relation to changes in eustasy (Uliana et al., 1999; Legarreta and Villar, 2015). These fluctuations restricted the sea bottom water circulation which temporarily favored euxinic conditions and the preservation and the accumulation of the OM (Legarreta and Uliana, 1991; Uliana et al., 1999). The studied mudstones were collected in the central basin from a borehole located in the thickest and deepest zone of the formation in the east of the fault system of Los Chihuidos (VMF-Well, Fig.1). Samples were collected between 2647 and 2808

meters and selected to cover a wide range of TOC throughout the thickness of the formation (Fig.2). These mudstones are considered to reach the gas window with a vitrinite reflectance (%Ro) of ~1.65% (Legarreta and Villar 2011).

The KCF consists of organic-rich marine mudstones alternating with marls developed from the Kimmeridgian to the Tithonian in several European basins (Figs.3, 4, Rawson and Riley, 1982; Herbin et al., 1991). The immature part of the formation outcrops in England, on the south coast (Dorset) and in Yorkshire (Fig.3). The studied samples were collected from two holes located in the Cleveland Basin, Marton and Ebberston (Yorkshire, England, Fig.3). These mudstones are characterized by high type II OM contents (2–30 wt.% of Rock-Eval® 6 TOC, Fig.4) accumulated in a shallow shelf regime under low energy and anoxic to suboxic conditions (Rawson and Riley, 1982; Herbin et al., 1991). These rocks have just reached the limit of the oil window with a vitrinite reflectance of ~0.5% (Ramanampisoa and Disnar, 1994). The formation is marked by pronounced cyclic variations in the OM content and quality (in terms of oil-proneness) related to climate and eustatic fluctuations at the Milankovitch scale (Oschmann, 1988; Ramanampisoa and Disnar, 1994; Desprairies et al., 1995; Boussafir et al., 1995a, b; Lallier-Vergès et al., 1995). According to these variations, different organic cycles of several orders have been distinguished by Oschmann (1988). The studied samples were selected in cycle I of Marton and Ebberston (Fig.4). The OM composition and its variations throughout this cycle were well-documented two decades ago (Oschmann 1988; Herbin et al., 1991; Ramanampisoa and Disnar, 1994; Boussafir et al., 1995a; Lallier-Vergès et al., 1995, 1997). This third-order cycle is characterized by facies variations (on a decametric to metric scale) from marly shales, mudstones, bituminous mudstones and coccolithic limestones (and conversely) in parallel with changes in the oxygenation of the dispositional environment and organic productivity (Oschmann 1988). While the organic-rich facies of the cycle contain mainly a marine and highly oil-prone phytoplanctonic OM, the others are composed of organic compounds with a lower quality for oil generation (Boussafir et al., 1995a; Lallier-Vergès et al., 1995, 1997). Marton and Ebberston samples were selected throughout the whole thickness of cycle I between 128.15-129.20 and 69.11-70.65 meters deep respectively (Fig.4) to cover a wide range of TOC and OM compositions.

2.2. Mineralogy and organic geochemistry

Rock-Eval pyrolysis is a classical method for determining the amount, type, HC-quality and maturity of OM preserved in source-rocks and sediments. Depending on the estimated OM content, 50 to 60 mg of dried sediment was used for new Rock-Eval 6® (Vinci Technologies, Rueil Malmaison) analysis. The pyrolysis program under inert gas (helium) started with an isothermal stage (2 min. 200°C). Then, the oven temperature was raised at 30 °C/min to 650 °C (held 3 min). The oxidation phase corresponds to an isothermal stage at 400 °C, then the temperature was raised at 30 °C min^{-1} to 850 °C (held 5 min) under purified air.

The significance of classical Rock-Eval parameters was explained by Espitalié et al. (1985a, b). The specific parameters given by the new Rock-Eval 6 device were presented by Lafargue et al. (1998). The Rock-Eval parameters used here were: (i) total organic carbon (TOC, wt.%), which expresses the quantity of OM calculated from the spectrum integration of S_1, S_2, S_3 (respectively, free hydrocarbons, pyrolizable hydrocarbons, CO and CO_2 produced by the breakdown of kerogen under inert gas flux), and S_4 peaks (CO and CO_2 produced by pyrolysis and oxidation of residual carbon under purified air flux); (ii) the hydrogen index (HI, mg HC /gTOC), i.e. the amount of hydrocarbon (HC) produced during pyrolysis (S_2); (iii) the oxygen index (OI, mg CO_2 /gTOC), which is calculated from the S_3 peak and represents the oxygenated quality of OM; (iv) T_{max}, a well-established OM maturity indicator (Espitalié et al., 1985a,b), that is the temperature of the maximum amount of hydrocarbons produced during pyrolysis.

Inorganic constituents were analyzed by X-ray diffraction (XRD) carried out on crushed samples (< 250 µm) under Cobalt radiation (INEL® diffractometer, CPS120 curved detector). The samples chosen for these analyses were selected throughout the entire Marton, Ebberston and VMF series to cover a wide range of depth and TOC contents. Relative mineral percentages were semi-quantified using the area under the curve for major diffraction peaks of each mineral and were then corrected using 4 artificial standard samples (laboratory mixtures with known abundances of mineral standards). This method, based on Fisher and Underwood (1995), assumes that there is a quantifiable relationship between peak area and the relative abundance of each mineral and that the factors are constant. This allows conversion from XRD to mineral abundances (Fisher and Underwood, 1995). The results were then normalized to 100% after TOC contents determined by Rock Eval pyrolysis.

Based on the analysis of standard samples, the reproducibility averaged ± 3.7 wt.% for quartz, ± 4.9 wt.% for total carbonate, ± 1.3 wt.% for pyrite, ± 3.2 wt.% for gypsum, ± 4.4 wt.% for total clay and ± 8.3 wt.% for albite.

2.3. Petrography

Petrographic observations were carried out on bulk rock polished sections (Leica® DMRX microscope) under oil immersion using reflected and UV-fluorescence light to identify the different macerals. VMF and KCF polished sections were made from small sample blocks impregnated with epoxy resin. The KCF thin sections used in this study were previously analyzed in Boussafir et al., 1995a; Boussafir and Lallier-Vergès, 1997. In the present study, palynofacies analysis (transmitted light microscopy under oil immersion) was carried out on KCF isolated OM and the associated metal sulphides of each sample (classical HF/HCI treatment, according to Boussafir et al., 1995a, b). This microscopical examination enabled the relative proportion of the organic components to be assessed.

Scanning electron microscope (SEM) observations were carried out on six polished thin sections using a SEM Merlin Zeiss® equipped with an in-lens secondary electron detector to image the samples' pore network. Two intermediary-TOC samples (~5.5 wt.%, Blc 23, Eb 30, Tab.1) and two relatively high-TOC samples (> 11.2 wt.%, Blc 30 Eb 40, Tab.1) were selected in Marton and Ebberston to ensure the representativeness of SEM observations throughout the KCF. For the VMF two samples with relatively high and representative TOC contents (94B, 5.0 wt.% and 102R, 6.7 wt.% Tab.1) were selected. These polished thin sections were first mechanically polished to facilitate broad beam argon-ion milling. Then, each section was milled through a two-step process. Thin sections were milled first using a source operated at 5 kV for 1 hour with a 4° tilt angle and a current of 220 µA, and then using a source operated at 2 kV for 30 min (220 µA). The thin sections were then coated with carbon to prevent electrostatic charging and improve the SEM image quality. Observations were conducted using backscattered (BSE) and secondary electrons (SE) under a current ranging from 10kV to 13 kV at a working distance of ~7.7 mm to 8.5 mm.

2.4. Pore structure

The total pore volume and the PSD of macropores and large mesopores were measured by mercury intrusion porosimetry (MIP) using a Micrometrics® Autopore IV 9500 porosimeter. About

1.5 g of sample was crushed into fragments (~2 mm in diameter), degassed under vacuum at 105°C for 24 h and intruded with mercury up to 60,000 psia (414 MPa). The equilibration time was set to 10 s. Penetrometers with a stem volume of 0.390 cm^3 were used for the analysis. The pore throat radius was calculated assuming cylindrical pores by the Laplace-Washburn equation (Washburn, 1921). Measurements were then corrected for conformance errors (Sigal, 2009, see in text).

Low-pressure nitrogen adsorption measurements were carried out on a Quantachrome® NOVA 2200^e apparatus at -196.15°C to measure the pore size distribution (PSD), the specific surface area and the volume of mesopores to large micropores. About 1 g of sample was powdered (<250 µm) and outgassed under vacuum at 105 °C for 24 h before analysis. Adsorption-desorption isotherms were obtained under the relative pressure P/Po ranging from 0.003 to 0.987. An equilibration time of 100 s was applied during the analysis. The total pore volume was determined after the liquid molar volume adsorbed at the relative pressure P/Po of 0.987. The specific surface area was determined using the Brunauer, Emmett and Teller method (BET) for adsorption in the best linear range between the relative pressure P/Po 0.03 and 0.33 (Brunauer et al., 1938). A minimum of 15 points was used for the BET surface-area analysis. The PSD was determined using the Barrett, Johner and Halenda (BJH) method (Barrett et al., 1951) applied from the adsorption isotherm to avoid tensile strength effect phenomena that occur during desorption. Note that the plot of dV/d(r) versus the pore diameter was preferred to the plot of dV/dlog(r) versus pore diameter to display the PSD. The plot of dV/dlog(r) versus the pore diameter is frequently used to display the PSD because it better shows the relative contribution of pores, over any ranges of pore sizes, to the total pore volume (Tian et al., 2013). The plot of dV/d(r) versus the pore diameter reflects, however, more accurately the concentrations of pores of various size, and provides thus, a complementary information to the plot of cumulated pore volume versus pore diameter (Tian et al., 2013). The pore volume and the specific surface area of micropores were calculated from the t-plot method using two models: the universal t-curve based on the Harkins-Jura model (De Boer et al., 1966) and the Carbon black model (Magee 1995; Tian et al., 2015). The Harkins-Jura model, the one most frequently used in the community, is based on standard siliceous materials (De Boer et al., 1966). Nevertheless, the Carbon black model is more specific for carbon-rich materials (Magee 1995) and should be more appropriate for the estimation of micropore volume

in gas-mature samples where the porosity is often associated with OM. The lowest detection limits for the pore volume and the specific surface area were 10^{-4} cm^3/g and 10^{-2} m^2/g respectively.

Clarkson et al., (2013) suggested that pore throats obtained by MIP are similar to pore bodies for some pore geometries including silt pores. In theory low-pressure nitrogen adsorption measurements and MIP should thus give similar results. Accordingly, pore throat size is often considered to be similar to pore size in shales (Wang et al., 2014). Kuila and Prasad (2011) showed that PSD curves from MIP and nitrogen adsorption exhibit a good correlation. Therefore, pore throat size from MIP was used as pore size in this study for convenience when comparing the nitrogen adsorption data.

3. Results

3.1. Mineralogy

Mineralogical data from XRD analysis are shown in Tab.2 and Fig.5. Quartz, calcite, clay minerals, feldspar and pyrite are the main mineral compounds in KCF and VMF samples (Tab.2, Fig.5). Both the VMF and the KCF formations show similar carbonate contents ranging from 6.6 to 29 wt.% ± 4.9 wt.% and relatively high pyrite contents (0.2–6.4 wt.% ± 1.3 wt.%, Tab.2). However, some differences can be noted. KCF samples are 10 to 20 wt.% richer in clay minerals (~53.0 wt.% ± 4.4 wt.%) than VMF rocks (~26.0 wt.% ± 4.4 wt.%, Tab.2, Fig.5) and are thus argillaceous mudstones. VMF samples which contain higher amounts of feldspar (~24.0 wt.% ± 8.3 wt.%) and quartz (28.0 wt.% ± 3.7 wt.%, Tab.2, Fig.5) are siliceous mudstones. Traces of gypsum are observed in KCF samples (Tab.2) as previously noted by Desprairies et al. (1995).

3.2. Organic geochemistry

Organic geochemistry data from Rock Eval pyrolysis are shown in Tab.1 and Fig.6 and their variations with depth are illustrated in Fig.7. All samples are organic-rich with TOC contents higher than 2 wt.% (Tab.1; Fig.7). VMF samples exhibit low S_2 (< 2.2 mg/g rock), HI (< 49 mg/g TOC) and OI (< 20 mg/g TOC) values regardless of TOC content (Tab.1; Fig.7C). As such, these samples plot near the origin in the pseudo-Van Krevelen diagram and the type of kerogen is non-identifiable (Fig.6). The high T_{max} values (~500°C) indicate a high maturity of OM corresponding to the gas window (Fig.6B, Fig.7C). The RC/TOC ratio is close to 1 (Tab.1), indicating the OM of VMF samples

is mainly composed of residual OM with a low residual petroleum potential (low HI and S_2 values) (Tab.1, Fig.7C).

The high HI (~527 mg/gTOC in Ebberston, ~452 mg/g in Marton) and low OI values (~20 mg/gTOC) of KCF samples show they are Type II kerogen (Tab.1, Fig.6A). The low production index (< 0.1) and T_{max} values (< 435°C) indicate their low maturity (Fig.6B). The RC/TOC ratio, far smaller than 1, (< 0.62), indicates that these samples contain a great fraction of pyrolizable OM (Tab.1). Consistent variations of TOC, HI and S_2 values are observed in KCF samples (Fig.7A and B). OI values exhibit a negative correlation with TOC in Marton (Fig.7B). Some very high-TOC samples (Eb 19, Eb 40 and Blc 30) exhibit higher pyrite contents (Tab.1 and Tab.2).

3.3. Petrographic observations

The results of petrographic observations are shown in Figs.8, 9 and 10 and SEM images are presented in Figs.11 and 12. In petrographic observations of VMF samples, OM is mainly comprised of highly reflective (grey) non-fluorescent granular particles often associated with pyrite or embayed against carbonate (Fig.8). Some of these particles show a fracture-filling texture (Fig.8B) or form abundant groundmass (Fig.8A) with pitted surface texture (Fig.8C). No identifiable biological structures are present, corroborating the high maturity of OM. These particles have been identified as secondary solid bitumen which is the dominant organic component in thermally mature organic-rich mudstones (Hackley and Cardott, 2016; Hackley, 2017). In SEM images, this residual OM appears as particles hosting nanometer-scale spongy pores (Figs.11F, H). A continuous spongy OM-hosted pore network is observed inside these carbon-rich residues (Fig.11). These spongy pores are abundant, closely spaced and exhibit subangular shapes (Figs.11E, H). The subangular spongy pores are the most abundant (Fig.11E, H) but many oval pores (bubble-like pores) are also observed (Fig.11 A, B, D). These OM-hosted pores appear to be mainly composed of mesopores and macropores with diameter smaller than 200 nm (Fig.11H); the larger pores probably come from the merging of smaller pores. Some pores are located between OM and mineral grains (Fig.11F). These mineral/OM pores cannot be classified as OM-hosted pores and are interpreted as mineral interparticle pores containing relics of OM. The residual porous OM is dispersed in a fine and compact mineral matrix, which appears in the SEM images to be mainly composed of clay mineral sheet aggregates, quartz and calcite grains

(Fig.11 Some interparticle macropores are located between quartz, calcite grains or clay-sheets (Fig.11) while some intraparticle macropores are located inside pyrite framboids and calcite grains (Figs.11C, D). Most of the clay mineral aggregates are located near the OM (Fig.11A, B, D). In these thermally-mature samples, only a few OM particles are non-porous or exhibit a low porosity (Fig.11G). Some devolatilization cracks were also observed in the OM (Fig.11B). Some of the large macropores (orange arrows, Fig.11) and the microfractures observed in these samples are interpreted as artefacts due to sample preparation.

KCF mudstones show a relatively heterogeneous OM distribution. In these immature samples, OM is composed of several terrestrial and marine macerals dispersed in a fine mineral matrix (Figs. 9 and 10). In SEM images, this mineral matrix appears to be composed of clay mineral aggregates, quartz, calcite-grains, pyrite framboids (Fig.12) and some microfossil remains (Fig.12 A, D, F). Terrestrial macerals, mainly represented by inertinite (Fig.9), form a large proportion of the structured OM (~15%, Fig.13). Phytoclasts, observed in palynofacies include some cuticular fragments, woody fragments and various debris of plant tissues (Fig.10 E–J). The predominant marine amorphous OM (AOM) (~75%) is supplemented by a minor contribution of structured organic components derived from preserved phytoplanktonic organic-walled and algal spores (~10%, Fig.13, Fig.10 K, L). This structured marine OM is present as brightly fluorescent thin bodies identified as *Tasmanite* spores (Fig.9). Three distinct types of AOM were identified: brown, orange and black AOM (Fig.10 A-D). Black AOM is the least abundant amorphous fraction (~10%, Fig.13). Brown AOM, identified as alginite in polished sections, is present as brightly fluorescent thin elongated bodies (yellow-colored under UV excitation, Fig.9). Orange AOM is generally associated with pyrite framboids (Fig.10A). In polished sections, these macerals are observable as thick elongated bodies oriented parallel to the bedding with a low brown/orange fluorescence (Fig.9). Abundant in high-TOC samples (Fig.9B, C), these organic particles, so called ‘bituminite’ (Kus et al., 2017), were previously described in the KCF (Boussafir et al., 1995b; Boussafir and Lallier-Vergès, 1997).

The abundance of these particles exhibits significant variations with TOC. In samples with TOC values < 6 wt.% the OM is rather composed of sparse fragments of inertinite with some alginites and rare *Tasmanite* algal bodies (Fig.9A). Samples with very high TOC values (> 6 wt.%) show an

increase in abundance of the fluorescent elongated organic particles including both alginites and bituminites (Fig.9B, C). After normalization with TOC, palynofacies observations show that orange AOM and pyrite contents dramatically increase with TOC and HI values (Fig.13; Tab.1) while brown and black AOM contents remain relatively stable (Fig.13). In SEM images, the OM is composed of elongated lamellar masses of kerogen particles (Fig.12). This OM constitutes a homogenous gel with well-defined boundaries cementing mineral grains, clay mineral sheets and pyrite framboids (Fig.12). Some horizontal fractures (Fr, Fig.12), shrinkage OM pores (Fig.12A) and rare OM-hosted mesopores with irregular shapes are visible (orange arrow, Ar, Fig.12). Such fractures and some of the OM-hosted pores are interpreted as artefacts due to sample preparation after retrieval from subsurface and thus may not be present in the subsurface (Chalmers et al., 2012; Tian et al., 2015). The OM in these low-mature samples is thus mainly non-porous. Most of the macropores and mesopores are < 4 µm in diameter and seem located between clay sheets, inside microfossil remains or between calcite, and quartz grains (Fig.12A, C, D). Some intraparticle pores are observed inside pyrite framboids (Fig.12B, E).

The relationships between TOC, quartz and clay mineral contents are shown in Fig.14. Clay mineral content exhibits no clear relationship with TOC contents in either of the formations (Fig.14). A negative linear correlation between TOC and quartz contents is observed in the VMF (R^2=0.70, Fig.14). A weaker negative linear correlation exists in the KCF between quartz and TOC (R^2=0.57, Fig.14). The relationships between organic carbon contents and the specific surface area are shown in Fig.15. VMF and KCF samples do not plot in the monolayer equivalent model trend such as Peru margin and Black-Sea sediments (Fig.15, Hedges and Keil, 1995). This model represents the quantity of organic carbon that can be contributed by organo-clay interactions as a function of the specific surface area. VMF and KCF sediments thus contain organic carbon that cannot have been contributed solely by organo-clay interactions. Compared with Peru margin and Black-Sea sediments, our results suggest that other additional mechanisms have allowed the OM to be well-preserved in the KCF and VMF formations (Hedges and Keil, 1995).

3.4. Porosity and pore size distribution

Data obtained from mercury intrusion porosimetry (MIP) are listed in Tab.3. MIP measurements revealed a connected total porosity ranging from 15.69 to 23.40% in the KCF and from 16.69 to 28.68% in the KCF (Tab.3). Cumulative intrusion as a function of TOC and PSD are shown in Fig.16 and Fig.17. A significant number of pores are located in the 50–1000 µm pore size range for the KCF sample and in the 100–1000 µm for the VMF samples (Fig.16 A, C). Nevertheless, these large macropores which largely contribute to the total porosity were never seen in SEM and petrographic observations. The largest pores imaged by SEM are about 6 µm in diameter in both formations. The presence of pores > 6 µm is considered as conformance errors due to surface roughness, cracks and filling of the container (Sigal, 2009; Klaver et al., 2012). In order to provide more realistic MIP data, mercury intrusion curves, porosity and pore volumes were thus corrected by excluding pores greater than 6 µm in diameter and by subtracting the first part of the intrusion data from the total (Fig.16 A, C). Corrected porosity and pore volumes are listed in Tab.3 and corrected PSD and cumulative intrusion curves are shown in Fig.17. After corrections, the total porosity ranges from 3.37 to 9.98% and the total pore volume ranges from 1.89 to 5.57 cm^3/100g for KCF samples (Tab.3). For VMF samples, their total porosities vary between 0.59 and 2.87% and the pore volume ranges from 0.35 to 1.63 cm^3/100g (Tab.3), suggesting a very low macro- and mesoporosity (>6 nm). The bulk and the skeletal density of all samples decrease with increasing TOC likely due to the difference in density between OM and minerals (Tab.3). KCF and VMF samples are mainly composed of mesopores less than 30 nm in diameter with a great number of pores measuring less than 15 nm (Fig.17). Only a few pores are in the 50 nm to 6 µm pore-size range in both formations (Fig.17). These macropores account for ~15.63% of the total pore volume in the KCF samples and for only ~ 7.71% in the VMF samples (Tab.3), suggesting a less abundant macroporosity in the VMF samples than in the KCF samples. The total pore volume and thus the porosity of KCF and VMF mudstones decrease with increasing TOC (Tab.3, Fig.16 B, D). KCF samples with more than 6 wt.% of TOC exhibit a lower number of pores in the 8 to 30 nm pore size range, and thus a lower porosity and total pore volume (Tab.3, Fig.16B, Fig.17). Nevertheless, these high-TOC samples can contain a significant amount of pores of less than 8 nm in diameter, such as Eb 19 or Eb 40 (Fig.17). However, some of these small pores may be due to the additional creation of pore space during the crushing process at a high

mercury pressure (up to 414 MPa) (Sigal, 2009; Comisky et al., 2011), and therefore these results must be interpreted with caution. VMF samples which contain more than 6 wt.% of TOC exhibit a lower porosity and total pore volume than samples with lower TOC contents due to a smaller number of mesopores in the 8–30 nm pore size range (Tab.3).

Data obtained from low-pressure nitrogen adsorption measurements are listed in Tab.4. The pore size distributions (PSD) are shown in Fig.18. VMF exhibits total pore volumes varying from 1.97 to 4.57 cm^3/g (Tab.4). In the KCF, total pore volumes range from 2.24 to 5.62 cm^3/g (Tab.4). The two models commonly used in the community for the t-plot method, the Harkins-Jura and the Carbon black models, provide comparable micropore surface areas and pore volumes (Tab.4). Although the Carbon black model is more specific for carbon-rich materials (Magee, 1995) and the Harkins-Jura model for siliceous materials (De Boer et al., 1966), the two models give similar results for these marine mudstones. This result suggests that these models are both useful t-plot models to evaluate micropore volume in marine mudstones and that their results can be easily compared. KCF samples exhibit low micropore volumes (< 0.50 $cm^3/100g$, Tab.4) and low specific surface areas (< 9.3 m^2/g, Tab.4). In these low-mature samples, micropores account for less than 15.2% of the total pore volume (Tab.4). VMF mudstones exhibit higher micropore volumes (0.50–1.10 $cm^3/100g$, Tab.4) and higher micropore specific surface areas (7.5–21.0 m^2/g, Tab.4), suggesting a higher microporosity. In these thermally-mature rocks, micropores account for 8.4 to 31.1% of the total pore volume (Tab.4). Despite this slightly higher microporosity in the VMF, total pore volumes of KCF and VMF are mainly provided by mesopores. Cumulative pore volumes show that the total pore volume is mainly provided by pores > 10 nm in diameter in both formations (Fig.18 D, E, F). PSD defined by low-pressure nitrogen adsorption analyses revealed that abundant micropores less than 8 nm are present in KCF and VMF samples (Fig.18 A, B, C), but have a low contribution to the total pore volume (Fig. 18 D, E, F). VMF samples show slightly higher specific surface areas than KCF samples (~21.0 m^2/g in the VMF, ~17.0 m^2/g in the KCF, Tab.4).

Total pore volumes and specific surface areas of KCF and VMF exhibit significant variations with TOC, but different trends are observed in the two formations (Fig.18, Fig.19 A, B, E, F). OM content exerts thus a strong control on porosity which depends on the thermal maturity of these marine

mudstones (Fig.19). In KCF samples, the specific surface area, the total pore volume (Fig.19 A, B) and the content of small mesopores and micropores (< 10 nm) decrease simultaneously with increasing TOC (Fig.17, Fig.18 B, C). Similar trends are observed for the cumulated pore volumes in the 10-100 nm pore size range (Fig.18 E, F), suggesting the decrease in the number of pores > 10 nm in diameter with increasing TOC. KCF samples can be divided into two groups according to the texture of clay minerals in SEM observations (Fig.19C, I, J). In lower clay samples, identified as group 1, phyllosilicate aggregates appear mainly isolated, dispersed in the mineral matrix with a more random orientation and accompanied by heterogeneous diffuse organo-mineral aggregates (Fig.19C, D, J). In clay rich-samples, identified as group 2, the phyllosilicate aggregates are parallel to each other, more compact, with some interlayer pores (Fig.19C, D, I). In this group, the OM is mainly composed of laminar pure OM without or with fewer insertions of clays. For both groups, the total pore volume strongly increases with quartz, carbonate and albite contents. In spite of the lower clay mineral contents of VMF samples, their specific surface area increases with increasing TOC content (Fig.19F). However, the evolution of pore volume as a function of TOC appears more complex since no relationship can be discerned between differential pore volumes and TOC contents (Fig.18 A, D). The total pore volume (Fig.19 E) and the cumulated pore volume (Fig18A) first increase with TOC contents but a lack of correlation is observed above 5.5 wt.%. That trend appears to be associated with the presence of smaller pores in organic-rich mudstones as evidenced by the decrease in the mesopore volume and the increase in the micropore volume above 5.5 wt.% of TOC (Fig.19E) and the high content of mesopores less than 2 nm in diameter in very high-TOC samples (Fig.18A). In contrast with low-mature samples, the total pore volume of VMF rocks exhibits no correlation with clay, quartz, feldspar and carbonate contents (Fig.19 G, H). Despite similar pore volumes and PSD, VMF and KCF mudstones exhibit therefore different pore characteristics.

4. Discussion

4.1. Organic petrography, porosity and pore size distribution

Petrographic and Rock Eval analysis show that KCF samples consist of low-mature organic-rich argillaceous mudstones with a high potential for oil generation (HI≈500 mg HC/g TOC, Tab.1, Figs.5, 6) while VMF samples consist of gas-mature siliceous mudstones mainly composed of a

residual OM with a low residual petroleum potential (RC/TOC > 0.90, low HI values, Tab.1, Figs.5, 6). This substantiates the %Ro of ~1.65% determined by Legarreta and Villar (2011) in the VMF and the %Ro of ~0.50% obtained by Ramanampisoa and Disnar (1994) in KCF mudstones. In KCF samples, the OM components identified in petrographic observations can be grouped into three classes according to their origin: (1) the brown AOM (alginite macerals) (Figs. 9, 10) which are derived from the selective preservation of resistant cell-walls of green microalgae and bacterial biomacromolecules (Largeau et al., 1984); (2) terrestrial particles including spores, woody and cuticular fragments and black AOM (Figs.9, 10) derived from bacterial macromolecules mixed with altered lignaceous debris (Boussafir and Lallier-Vergès, 1997); (3) the orange AOM interpreted as bituminite macerals (Figs.9, 10, Boussafir et al., 1995b; Boussafir and Lallier-Vergès, 1997).

Previous studies suggest that these macerals have high hydrocarbon potentials and nanoscopically amorphous and homogeneous ultrafine structures in TEM observations, and are derived from phytoplanktonic lipidic remains preserved by natural vulcanization (Ramanampisoa and Disnar, 1994; Boussafir et al., 1995b; Boussafir and Lallier-Vergès, 1997). In the KCF, periods of high productivity allow the metabolizable OM to enter the anoxic zone, favoring the development of sulphate-reducing organisms and thus the production of H_2S (Lallier-Vergès et al., 1995; Boussafir et al., 1995a; Boussafir and Lallier-Vergès, 1997). Most of this H_2S diffuses from the sea sediments, while a part reacts with the reactive metals present in sediments to form sulphides (commonly pyrite) (Boussafir et al., 1995a; Boussafir and Lallier-Vergès, 1997). The excess of H_2S is then in part incorporated as organosulfur compounds in the metabolizable OM by natural vulcanization to form bioresistant amorphous OM known as orange AOM (Boussafir and Lallier-Vergès 1997). These processes of natural sulfurization have allowed the preservation of a large amount of metabolizable OM explaining why KCF mudstones are not close to the monolayer equivalent field in the TOC versus specific surface area diagram (Fig.15). Furthermore, this also explains the strong association of these hydrogen-rich amorphous OM with pyrite (Figs.9, 10, 13) and the relative increase of the OM quality in terms of oil-proneness with increasing TOC (Tab.1, Fig.13). In SEM images, such OM exhibits a homogenous and gelified texture with well-defined boundaries and manifests a very low primary porosity (Fig.12). In the high-TOC samples (≥ 5.4 wt.%, Tab.1), the amorphous OM represents more

than 85% of TOC based on observations with SEM (Fig.13). These amorphous and homogeneous particles have lost their inherited biological structure due to reorganizations during preservation processes (Boussafir and Lallier-Vergès, 1997; Boussafir et al., 1995a and b), probably explaining their low primary porosity. Furthermore, the increase in the pore volume, the porosity and the specific surface area with decreasing TOC (Fig.16B, Fig.17B-F, Fig.18B-F) suggests that the porosity of these low-mature mudstones is not provided by these rare OM-hosted pores. On the contrary, the gel formed by this amorphous OM appears to fill the interparticle mineral porosity, reducing the pore volume (Fig.12, Fig.19A, B). Most of the porosity in these low-mature rocks is thus composed of mineral-associated pores which are not filled by OM (Fig.12). The strong increase in the pore volume with quartz, calcite and albite contents (Fig.19D) indicates that the pores located between mineral grains (Fig.12) largely contribute to the total porosity. Nevertheless, the behavior of the pore volume as a function of quartz, calcite and albite contents seems to be influenced by the texture of the clay minerals (Fig.19C, D, I, J). The slightly higher clay mineral contents of group 2 (Fig.19C) seem to have favored the presence of thick phyllosilicate aggregates, parallel to each other, more compact, with some interlayer pores (Fig.19I). In samples with relatively low clay mineral contents (group 1), clay minerals, mainly isolated, dispersed in the mineral matrix with a more random orientation and with the presence of heterogeneous diffuse organo-mineral aggregates appear to be less favorable to the presence of interlayer-pores between them (Fig.19J). This observation suggests that clay mineral texture can influence the porosity of low-mature marine mudstones. However, the origin of this difference of texture and the link with clay mineral contents is unclear and further investigations are required.

VMF samples exhibit very different features. The generation of hydrocarbons with increasing maturity has led to the formation of a residual OM identified as secondary solid bitumen (Fig.8). This carbon-rich residue (often called pyrobitumen) was probably formed during the secondary cracking of liquid oil into gas (Tissot and Welte, 1984; Lewan, 1993; Behar et al., 1997; Bernard et al., 2012; Reed et al., 2014). The large predominance of pyrobitumen was previously noted in most thermally mature mudstones (Bernard et al., 2012; Hackley and Cardott, 2016; Hackley, 2017). In SEM and

petrographic observations, this “grainy” OM exhibits a highly-developed and interconnected OM-hosted porosity compared to the KCF immature organic “gel” (Figs.11, 12). These nanometer-size OM-hosted pores exhibit variable shapes (Fig.11). While most of them are subangular spongy OM pores, abundant oval pores (bubble-like) are visible in some OM particles (Fig.11). Similar pores have been commonly described in thermally-mature mudstone reservoirs (Loucks et al., 2012; Curtis et al., 2012; Bernard et al., 2012; Hackley and Cardott 2016; Ko et al., 2016, 2017). These oval and subangular spongy pores are often considered to be formed in secondary solid bitumen/or pyrobitumen during gas generation and expulsion from the end of the oil window to the dry gas zone (Bernard et al., 2012; Ko et al., 2016). Not all the OM in the VMF is porous: some sparse and rare OM particles, probably kerogen (inertinite) are non-porous or exhibit a very low porosity (Fig.12G). Similar observations were made in thermally mature KCF, Woodford and Marcellus mudstones (Fishman et al., 2012; Curtis et al., 2012; Hackley and Cardott, 2016), suggesting that residual kerogen evolves differently from pyrobitumen with increasing maturity. Contrary to the KCF, the strong increase in the specific surface area with TOC (Fig.19F) demonstrates that the porosity of gas-mature mudstones is mainly provided by these OM-hosted pores. On the contrary, the absence of correlation between TOC and mineral contents (Fig.19G, H) suggests that the interparticle pores identified between clay sheets, calcite and quartz grains (Fig.8) do not significantly contribute to the pore volume.

OM from the thermally mature VMF rocks is dominated by secondary solid bitumen (Figs.8, 12). Due to the high maturity of these samples, this precursor OM is unidentifiable but previous studies have shown the presence of a KCF-like type II OM (Uliana et al., 1999; Legarreta and Villar, 2011, 2015). OM of low-mature VMF mudstones is mainly composed of hydrogen-rich type II OM derived from the early diagenesis of phytoplankton and algal bacterial contributions (orange and brown AOM observed in KCF) with variable amounts of alginite and terrestrial relics (Uliana et al., 1999; Legarreta and Villar, 2011, 2015). Highly oil-prone amorphous OM content increases with TOC content (3 to 12 wt.%, Legarreta and Villar, 2011, 2015), leading to fluctuations of HI (≈ 650 mg HC/g TOC, Legarreta and Villar, 2011, 2015) and OI (< 30–40 mg CO_2/g TOC, Legarreta and Villar, 2011, 2015) as a function of TOC as observed in KCF mudstones (Tab.1). Therefore, in the present study VMF and KCF mudstones exhibit: (1) similar high pyrite contents which attests to natural

sulfurization processes (Tab.2); (2) a similar absence of correlation between clay and TOC contents (Fig.14); (3) similar high TOC contents compared to their specific surface areas (Fig.15, Hedges and Keil, 1995) showing the low contribution of organo-clay interactions regardless of vulcanization (orange AOM) and selective preservation processes (brown AOM). These formations thus contain two different stages of maturity of the similar precursor organic material which may allow comparison of their OM-hosted porosity as a function of maturity.

Previous work has demonstrated that clay minerals can act as catalysts in the acid-catalyzed cracking of kerogen into hydrocarbons during thermal maturation (Tannenbaum and Kaplan, 1985; Pan et al., 2009). Differences in clay mineral contents appear to mainly influence the kinetics of hydrocarbon generation during the low stage of maturation (Tannenbaum and Kaplan, 1985). We can assume that variations in clay mineral content may lead to a different evolution of OM porosity in some formations during the oil generation stage. The catalytic influence of clays is, however, minor in higher maturation stage such as the gas window for our VMF samples (Tannenbaum and Kaplan, 1985). However, if we admit some catalytic effect in this higher maturation stage, and despite the lower clay mineral content of the Vaca Muerta samples (Tab.2, Fig.5), most of the OM is integrated with or closely associated to clay mineral aggregates (Fig.11A, B and D) as for the KCF. We can therefore assume that the catalytic effect of clay might be similar in the KCF and VMF formations and that the difference in mineralogy between these formations probably had a limited impact on OM porosity in these gas-mature samples.

4.2. Thermal maturity involvement in OM-hosted pore genesis

With a pore volume ranging between 2.0 and 5.6 $cm^3/100g$ (Tab. 4), KCF and VMF samples exhibit a good storage capacity. The hydrous pyrolysis experiments of Chen and Xiao (2014) suggest that porosity and pore volumes increase with increasing maturity and thus thermally-mature mudstones will exhibit a higher porosity than low-mature rocks. Surprisingly, pore volumes determined from nitrogen adsorption show similar trends for both formations despite their difference in maturity (Tab.4). This observation suggests that the relationship between thermal maturity and total pore volume is not straightforward.

The porosity of both formations appears to be mainly mesoporous. The few number of mesopores in the 7-100 nm pore size range account for the most part of the pore volume (Fig.18). KCF and VMF samples contain, however, abundant mesopores and micropores less than 8 nm in diameter which have a low contribution to the total pore volume (Figs.17, 18). The presence of these very small mesopores (< 8 nm) and micropores has been previously noted in many gas shale systems (Chalmers and Bustin, 2008; Chalmers et al., 2012; Tian et al., 2015). The contribution of micropores to the total pore volume determined from nitrogen adsorption is higher in thermally-mature VMF mudstones (~21.0%) than in the KCF (~4.9 - 8.7%, Tab.4). MIP measurements reveal that the macropores observed in SEM images do not greatly contribute to the porosity of KCF (10.6-22.8%, Tab.3) and VMF mudstones (Figs.11, 12 and 17). This may explain the low porosity and the low pore volumes of VMF samples measured using MIP (Tab.3): the main part of the porosity of these thermally-mature mudstones is below the detection limit of MIP measurements. This was especially true for VMF samples in which macropores account for less than 9% of the total pore volume obtained by MIP (Tab.4). Moreover, VMF samples show slightly higher specific surface areas (Tab.4). This result is quite surprising in view of the mineralogical compositions of these two series. Contrary to the observations, the higher content of clay minerals in KCF samples (Fig.5) is expected to give them a greater specific surface area. This difference is likely related to the greater microporosity of VMF samples. This suggests a greater contribution in the KCF of the macropores observed between mineral grains and clay mineral aggregates in SEM images (Fig.12). The higher thermal maturity and the greater depth of gas-mature samples have probably allowed a greater mineral matrix compaction than in low-mature KCF mudstones, thus probably reducing the number of macropores. Moreover, the presence of some mineral/OM pores and abundant solid bitumen (Figs.8, 11) suggests that the original mineral pores were partially filled during petroleum generation. Located between mineral grains (Fig.11F), these ‘modified mineral pores’ are considered as original mineral pores, filled first by petroleum which was later extracted leaving behind residual solid bitumen and smaller pores (Ko et al., 2016, 2017). It can therefore be assumed that this process has also contributed to the progressive decrease in the number of primary macropores in thermally-mature samples.

The more fully developed spongy OM-hosted pores in gas-mature rocks suggests that they are essentially controlled by thermal maturation. This observation substantiates the common model of organic-hosted pore genesis which holds that the porosity increases during maturation in response to the volume lost during expulsion of the liquid and gaseous hydrocarbons produced by the thermal primary and secondary cracking of the OM (Jarvie et al., 2007; Chalmers and Bustin, 2008; Loucks et al., 2012; Curtis et al., 2012). Recent studies show that these OM-hosted pores first formed in solid bitumen since the oil window (Juliao et al., 2015; Ko et al., 2016; Hackley and Cardott 2016) may further developed progressively to the dry gas zone and become predominant in gas-mature mudstones such as the VMF samples (Jarvie et al., 2007; Chalmers and Bustin, 2008; Loucks et al., 2012; Curtis et al., 2012; Chen and Xiao, 2014; Hackley, 2017; Ko et al., 2018). Nevertheless, while OM appears to be the major contributor to the total pore volume of these thermally-mature mudstones, the total pore volume does not increase linearly with TOC (Fig.19E). This suggests that other factors than maturity are working.

While the OM-hosted porosity increases strongly with thermal maturity (Curtis et al., 2012; Loucks et al., 2012; Chen and Xiao, 2014; Ko et al., 2017; Hackley, 2017), this gain in volume may be counteracted by the decrease in the interparticle pores by compaction and diagenetic processes (Charpentier et al., 2003; Day-Stirrat et al., 2008; Milliken et al., 2013). The combination of these processes may not lead to a systematic variation in the total pore volume as a function of thermal maturity (Tab.3). Consequently, TOC may sometimes have a stronger control on these parameters than thermal maturity as previously observed in other studies (Milliken et al., 2013; Pan et al., 2015).

4.3. Secondary OM-hosted pores vs primary organic porosity

In contrast with SEM observations in low-mature KCF mudstones which reveal a very low primary OM-hosted porosity, the presence of very porous OM in immature to low-mature samples (Ro: 0.35-0.50%) has been previously noted in the Woodford shale, in the Monterey or in Stuart Range formations (Löhr et al., 2015). This suggests that some specific OM may contain abundant primary OM-hosted pores inherited from their biological structure. Similar observations were recently made in the Eagle Ford, the Wilcox group and the Smithwick shales (Reed, 2017). Reed (2017)

suggested that this primary OM porosity is closely tied to the presence of terrestrial organic matter, probably inherited from the original structures of cellulose and woody fragments. The low content of these terrestrial organic materials in KCF samples (less than 15% of the TOC, Fig.13) and the small area covered by SEM images probably may not allow the observation of these porous OM in the present study. Furthermore, even if we assume that non-observed primary OM-hosted pores exist in low-mature KCF mudstones, these pores do not significantly contribute to the total pore volume, as shown by the decrease in porosity, the total pore volume and the specific surface area with increasing TOC (Fig.16B, Fig.19A).

While the difference in OM-hosted porosity between low-mature KCF and thermally-mature VMF mudstones is clearly illustrated in the present study, Fishman et al. (2012) demonstrated that in the offshore KCF mudstones, the size and abundance of this primary porosity varies with the maceral composition but is largely similar regardless of maturity variation between 0.5–1.3%Ro. Similar observations were also noted in the Woodford shale, in the Monterey or the Stuart Ranges formations (Löhr et al., 2015). A hypothesis can be proposed to explain this difference with gas-mature rocks from the VMF. As suggested by Fishman et al. (2012), the plastic nature of the clay-rich KCF mudstones (Tab.2, Fig.5) could allow a greater compaction of pores developed during hydrocarbon generation. The secondary OM porosity in KCF mudstones may thus have not been preserved like the VMF mudstones which exhibit a higher content of rigid minerals (quartz and feldspar, Tab.1, Fig.3) and allow a better preservation of pores during compaction (Day-Stirrat et al., 2008; Schieber, 2010). Nevertheless, further investigations are needed to understand the connections which may exist between mineral compositions, compaction and secondary OM-hosted pores.

4.4. TOC and OM composition controls on pore genesis

Although thermal maturation appears to have significant effect on OM-hosted genesis, this process alone is insufficient to explain the decrease in the pore size with increasing TOC in thermally-VMF mature samples with TOC values greater than 5.5 wt.% (Fig.19E). Similar trends were also previously observed in Marcellus mudstones (Milliken et al., 2013) and the Permian mudstones of the Lower Yangtze region (Pan et al., 2015). This observation may explain the lower pore volumes and

MIP porosity of the two very high-TOC samples (7.3 wt% and 9.1 wt.%, Fig.16D). Contrary to the lower-TOC samples (< 5.5 wt.%) which contain larger pores, the main part of the porosity of these high-TOC samples (> 5.5 wt.%) is below the detection limit of MIP. These samples contain a higher proportion of mesopores and macropores below the MIP detection limit (Tab.3). The difference in the OM composition between high- and low-TOC samples could explain these pore-size variations as a function of TOC. In KCF mudstones, the increase of orange AOM content is responsible for higher values of HI and petroleum potential (S_2) and corresponds to periods of anoxia favorable to natural sulfurization processes (Boussafir et al., 1995a). These periods are marked by slightly lower quartz content (Fig.14). By comparison, low-TOC samples correspond to periods marked by a greater proportion of quartz and terrestrial OM inputs (Figs.13, 14), responsible for the decrease in the OM quality with respect to oil generation and in the TOC content (Fig.7 A, B). Similar variations were previously documented in low-mature VMF mudstones (Legarreta and Uliana, 1991; Uliana et al., 1999; Legarreta and Villar, 2011, 2015). Similar variations in the original OM composition as a function of TOC can thus be expected in VMF mudstones and three explanations can be suggested: (1) As previously mentioned (Milliken et al., 2013; Pan et al., 2015), the smallest OM-pores of organic rich samples may represent a more complete pore network collapse after petroleum migration caused by a higher hydrocarbon production (or higher petroleum potential); (2) Alternatively, higher TOC samples from the VMF probably contained a greater content of well-preserved highly oil-prone OM which are less prone to the production of large *in-situ* OM mesopores during maturation. Well-preserved and more hydrogen-rich type II macerals (e.g., high HI values) produce liquid hydrocarbons, richer in light constituents, that are easy to migrate outward while more degraded and less oil-prone (e.g., low HI values) type II macerals produce heavier and more viscous oils (richer in asphaltenes, Tissot and Welte, 1984). During the secondary cracking of these viscous oils, abundant secondary solid bitumens and essentially gaseous HC are produced, which may result in a greater amount of mesoporosity. This may explain why TOC and pore volume are not systematically positively correlated. Moreover, some macerals such as inertinite (Fig.11G) do not appear to develop pores with increasing maturity. This may explain the variations in porosity observed between nearby organic regions of the same sample in Woodford mudstones (Curtis et al., 2012). Changes in the

relative proportion of these non-porous macerals may thus explain some variations between these samples. The importance of maceral types has been previously emphasized to explain porosity variations (Fishman et al., 2012; Loucks et al., 2012; Milliken et al., 2013; Cardott et al., 2015; Ko et al., 2017, 2018); (3) A close link seems to exist between the production of gas and OM-hosted pore genesis from the oil window to the dry gas zone (Bernard et al., 2012; Milliken et al., 2013). Spongy pores in thermally-mature samples seem form from the nucleation and the expulsion of gaseous hydrocarbons produced by the thermal cracking of OM (Chalmers and Bustin, 2008; Loucks et al., 2012; Curtis et al., 2012; Bernard et al., 2012; Milliken et al., 2013). Moreover, artificial maturation experiments have shown that the quantity of gas (CO, CO_2, CH_4,C_2-C_5) generated during the thermal diagenesis of OM can vary greatly between type I, II or III kerogen (Behar et al., 1992; Behar et al., 1997). It may be appropriate to assume that slight fluctuations in the OM composition may have led to the production of various quantity of gas during thermal maturation resulting in variations of the amount of spongy pores formed in residual OM between samples. This may explain in part why high- and low-TOC samples in the VMF exhibit different pore sizes.

In gas shale systems composed of a heterogeneous OM, this different evolution of OM porosity during maturation may mask the effect of thermal maturity. That could explain why porosity appears to be mainly controlled by TOC in some formations such as the Marcellus (Milliken et al., 2013) or in the Lower Yangtze region (Pan et al., 2015) and suggests therefore that thermal maturity and OM composition have a complementary effect, explaining the complexity and the diversity of trends observed in natural gas shale systems.

5. Summary and conclusions

The pore structure and the geochemistry of rocks from the Kimmeridge Clay Formation and the Vaca Muerta Formation were investigated and the following conclusions are drawn.

- KCF rocks are low-mature marine mudstones mainly composed of amorphous and less-porous marine OM while VMF samples are gas-mature marine mudstones mainly composed of porous secondary solid bitumen.

- The OM composition of KCF samples manifests variations. High-TOC samples contain higher lipidic phytoplanktonic fractions and thus have a higher petroleum potential than low-TOC samples. Similar variations were observed in low-mature VMF mudstones.
- Pore size distributions show a predominance of pores smaller than 30 nm and the pore volume ranges between 2 and 5 cm^3/100g regardless of the degree of maturity. Nevertheless, pore networks in gas shale vary significantly with thermal maturity. The porosity of low-mature mudstones is dominated by inorganic interparticle pores while the main contributor to the porosity of thermally mature rocks is the porous secondary solid bitumen. OM porosity, low in the immature stage, appears to be formed in solid bitumen and increases during thermal diagenesis in response to hydrocarbon generation, becoming predominant in thermally mature rocks.
- Although the porosity of gas-mature mudstones is mainly controlled by OM, surprisingly no linear correlation is observed between TOC and total pore volume for samples with TOC greater than 5.5 wt.%. This observation appears to be tied to the decrease of the number of pores with increasing TOC. Differences in the composition of the precursor OM between high- and low-TOC samples may explain these pore-size variations. This suggests that other controlling factors such as OM composition can influence OM-hosted pore genesis. Three hypotheses can be put forward: (1) a stronger framework compaction of high-TOC samples in response to volume lost during the expulsion of a greater amount of hydrocarbons (higher petroleum potential); 2) The presence of well-preserved and more hydrogen-riche type II OM in high-TOC samples that is less favorable to the production of viscous oils and abundant porous secondary solid bitumen and thus less favorable to the formation of large mesopores (3) Variations in the quantity of gas generated during thermal maturation due to different composition of the precursor OM between high- and low-TOC samples may have led to variations in the quantity of pores formed in residual OM in response to gas nucleation and expulsion.

Acknowledgements

We would like to thank Mr. Philippe Penhoud for his expert support of the XRD analysis, Mrs. Ida Di Carlo for guidance on sample preparation and SEM BSE and SE analysis and Mrs. Rachel Boscardin for her assistance in the laboratory. Special thanks go to Mrs. Elizabeth Rowley-Jolivet for her excellent proofreading as a native speaker of English and linguist. Finally, we would like to thank Mr. Paul Hackley and the anonymous reviewers for their recommendations that have greatly improved the manuscript.

References

Barrett, E. P., Joyner, L. G., & Halenda, P. P. (1951). The determination of pore volume and area distributions in porous substances. I. Computations from nitrogen isotherms. *Journal of the American Chemical society*, *73*(1), 373-380.

Behar, F., Kressmann, S., Rudkiewicz, J. L., & Vandenbroucke, M. (1992). Experimental simulation in a confined system and kinetic modelling of kerogen and oil cracking. *Organic Geochemistry*, *19*(1-3), 173-189.

Behar, F., Vandenbroucke, M., Tang, Y., Marquis, F., & Espitalie, J. (1997). Thermal cracking of kerogen in open and closed systems: determination of kinetic parameters and stoichiometric coefficients for oil and gas generation. *Organic Geochemistry*, *26*(5-6), 321-339.

Bernard, S., Wirth, R., Schreiber, A., Schulz, H. M., & Horsfield, B. (2012). Formation of nanoporous pyrobitumen residues during maturation of the Barnett Shale (Fort Worth Basin). *International Journal of Coal Geology*, *103*, 3-11.

Boussafir, M., Gelin, F., Lallier-Verges, E., Derenne, S., Bertrand, P., & Largeau, C. (1995a). Electron microscopy and pyrolysis of kerogens from the Kimmeridge Clay Formation, UK: Source organisms, preservation processes, and origin of microcycles. *Geochimica et Cosmochimica Acta*, *59*(18), 3731-3747.

Boussafir, M., Lallier-Vergès, E., Bertrand, P., & Badaut-Trauth, D. (1995b). SEM and TEM studies on isolated organic matter and rock microfacies from a short-term organic cycle of the Kimmeridge Clay Formation (Yorkshire, GB). In *Organic Matter Accumulation* (pp. 15-30). Springer, Berlin, Heidelberg.

Boussafir, M., & Lallier-Vergès, E. (1997). Accumulation of organic matter in the Kimmeridge Clay Formation (KCF): an update fossilisation model for marine petroleum source-rocks. *Marine and petroleum geology*, *14*(1), 75-83.

Brunauer, S., Emmett, P. H., & Teller, E. (1938). Adsorption of gases in multimolecular layers. *Journal of the American chemical society*, *60*(2), 309-319.

Cardott, B. J., Landis, C. R., & Curtis, M. E. (2015). Post-oil solid bitumen network in the Woodford Shale, USA—A potential primary migration pathway. *International Journal of Coal Geology*, *139*, 106-113.

Chalmers, G. R., & Bustin, R. M. (2008). Lower Cretaceous gas shales in northeastern British Columbia, Part I: geological controls on methane sorption capacity. *Bulletin of Canadian petroleum geology*, *56*(1), 1-21.

Chalmers, G. R., Bustin, R. M., & Power, I. M. (2012). Characterization of gas shale pore systems by porosimetry, pycnometry, surface area, and field emission scanning electron microscopy/transmission electron microscopy image analyses: Examples from the Barnett, Woodford, Haynesville, Marcellus, and Doig units. *AAPG bulletin*, *96*(6), 1099-1119.

Charpentier, D., Worden, R. H., Dillon, C. G., & Aplin, A. C. (2003). Fabric development and the smectite to illite transition in Gulf of Mexico mudstones: an image analysis approach. *Journal of Geochemical Exploration*, *78*, 459-463.

Chen, J., & Xiao, X. (2014). Evolution of nanoporosity in organic-rich shales during thermal maturation. *Fuel*, *129*, 173-181.

Clarkson, C. R., Solano, N., Bustin, R. M., Bustin, A. M. M., Chalmers, G. R. L., He, L., Melnichenko, Y.B., Radlinski, A.P., & Blach, T. P. (2013). Pore structure characterization of North American shale gas reservoirs using USANS/SANS, gas adsorption, and mercury intrusion. *Fuel*, *103*, 606-616.

Comisky, J. T., Santiago, M., McCollom, B., Buddhala, A., & Newsham, K. E. (2011, January). Sample size effects on the application of mercury injection capillary pressure for determining the storage capacity of tight gas and oil shales. In *Canadian unconventional resources conference*. Society of Petroleum Engineers.

Curtis, M. E., Cardott, B. J., Sondergeld, C. H., & Rai, C. S. (2012). Development of organic porosity in the Woodford Shale with increasing thermal maturity. *International Journal of Coal Geology*, *103*, 26-31.

Day-Stirrat, R. J., Aplin, A. C., Środoń, J., & Van der Pluijm, B. A. (2008). Diagenetic reorientation of phyllosilicate minerals in Paleogene mudstones of the Podhale Basin, southern Poland. *Clays and Clay Minerals*, *56*(1), 100-111.

De Boer, J. H., Lippens, B. C., Linsen, B. G., Broekhoff, J. C. P., Van den Heuvel, A., & Osinga, T. J. (1966). Thet-curve of multimolecular N2-adsorption. *Journal of Colloid and Interface Science*, *21*(4), 405-414.

Desprairies, A., Bachaoui, M., Ramdani, A., & Tribovillard, N. (1995). Clay diagenesis in organic-rich cycles from the Kimmeridge Clay Formation of Yorkshire (GB): implication for palaeoclimatic interpretations. In *Organic Matter Accumulation* (pp. 63-91). Springer, Berlin, Heidelberg.

Espitalie, J., Deroo, G., & Marquis, F. (1985a). Rock-Eval pyrolysis and its applications. *Revue De L Institut Francais Du Petrole*, *40*(5), 563-579.

Espitalie, J., Deroo, G., & Marquis, F. (1985b). Rock-Eval pyrolysis and its applications 2. *Revue De L Institut Francais Du Petrole*, *40*(6), 755-784.

Fisher, A. T., & Underwood, M. B. (1995). Calibration of an X-ray diffraction method to determine relative mineral abundances in bulk powders using matrix singular value decomposition: a test from the Barbados accretionary complex. In *Proceedings of the Ocean Drilling Program. Initial reports*, *156*, 29-37.

Fishman, N. S., Hackley, P. C., Lowers, H. A., Hill, R. J., Egenhoff, S. O., Eberl, D. D., & Blum, A. E. (2012). The nature of porosity in organic-rich mudstones of the Upper Jurassic Kimmeridge Clay Formation, North Sea, offshore United Kingdom. *International Journal of Coal Geology*, *103*, 32-50.

Garcia, M. N., Sorenson, F., Bonapace, J. C., Motta, F., Bajuk, C., & Stockman, H. (2013, August). Vaca Muerta Shale reservoir characterization and description: The starting point for development of a Shale play with very good possibilities for a successful project. In *Unconventional Resources Technology Conference* (pp. 863-899). Society of Exploration Geophysicists, American Association of Petroleum Geologists, Society of Petroleum Engineers.

Hackley, P. C., & Cardott, B. J. (2016). Application of organic petrography in North American shale petroleum systems: A review. *International Journal of Coal Geology*, *163*, 8-51.

Hackley, P.C. (2017). Application of Organic Petrology in High Maturity Shale Gas Systems.*Geology: Current and Future Developments*, 2017, *Vol. 1*, 3-38.

Hedges, J. I., & Keil, R. G. (1995). Sedimentary organic matter preservation: an assessment and speculative synthesis. *Marine chemistry*, *49*(2-3), 81-115.

Herbin, J. P., Muller, C., Geyssant, J. R., Mélières, F., & Penn, I. E. (1991). Hétérogénéité quantitative et qualitative de la matiére organique dand les argiles du Kimméridgien du Val de Pickering (Yorkshire, UK): cadre sédimentologique et stratigraphique. *Revue de l'Institut français du pétrole*, *46*(6), 675-712.

Howell, J. A., Schwarz, E., Spalletti, L. A., & Veiga, G. D. (2005). The Neuquén basin: an overview. *Geological Society, London, Special Publications*, *252*(1), 1-14.

Jarvie, D. M., Hill, R. J., Ruble, T. E., & Pollastro, R. M. (2007). Unconventional shale-gas systems: The Mississippian Barnett Shale of north-central Texas as one model for thermogenic shale-gas assessment. *AAPG bulletin*, *91*(4), 475-499.

Juliao, T., Suárez-Ruiz, I., Marquez, R., & Ruiz, B. (2015). The role of solid bitumen in the development of porosity in shale oil reservoir rocks of the Upper Cretaceous in Colombia. *International Journal of Coal Geology*, *147*, 126-144.

Katz, B. J., & Arango, I. (2018). Organic Porosity: A Geochemist's View of the Current State of Understanding. *Organic Geochemistry*.

Kietzmann, D. A., Martin-Chivelet, J., Palma, R. M., López-Gómez, J., Lescano, M., & Concheyro, A. (2011). Evidence of precessional and eccentricity orbital cycles in a Tithonian source rock: the mid-outer carbonate ramp of the Vaca Muerta Formation, Northern Neuquén Basin, Argentina. *AAPG bulletin*, *95*(9), 1459-1474.

Kietzmann, D. A., Palma, R. M., Riccardi, A. C., Martín-Chivelet, J., & López-Gómez, J. (2014). Sedimentology and sequence stratigraphy of a Tithonian–Valanginian carbonate ramp (Vaca Muerta Formation): A misunderstood exceptional source rock in the Southern Mendoza area of the Neuquén Basin, Argentina. *Sedimentary Geology*, *302*, 64-86.

Kietzmann, D. A., Ambrosio, A. L., Suriano, J., Alonso, M. S., Tomassini, F. G., Depine, G., & Repol, D. (2016). The Vaca Muerta–Quintuco system (Tithonian–Valanginian) in the Neuquén Basin, Argentina: A view from the outcrops in the Chos Malal fold and thrust belt. *AAPG Bulletin*, *100*(5), 743-771.

Klaver, J., Desbois, G., Urai, J. L., & Littke, R. (2012). BIB-SEM study of the pore space morphology in early mature Posidonia Shale from the Hils area, Germany. *International Journal of Coal Geology*, *103*, 12-25.

Ko, L. T., Loucks, R. G., Zhang, T., Ruppel, S. C., & Shao, D. (2016). Pore and pore network evolution of Upper Cretaceous Boquillas (Eagle Ford–equivalent) mudrocks: Results from gold tube pyrolysis experiments. *AAPG Bulletin*, *100*(11), 1693-1722.

Ko, L. T., Loucks, R. G., Milliken, K. L., Liang, Q., Zhang, T., Sun, X., ... & Peng, S. (2017). Controls on pore types and pore-size distribution in the Upper Triassic Yanchang Formation, Ordos Basin, China: Implications for pore-evolution models of lacustrine mudrocks. *Interpretation*, *5*(2), SF127-SF148.

Ko, L. T., Ruppel, S. C., Loucks, R. G., Hackley, P. C., Zhang, T., & Shao, D. (2018). Pore-types and pore-network evolution in Upper Devonian-Lower Mississippian Woodford and Mississippian Barnett mudstones: Insights from laboratory thermal maturation and organic petrology. *International Journal of Coal Geology*, *190*, 3-28.

Kuila, U., & Prasad, M. (2011, January). Understanding pore-structure and permeability in shales. In *SPE Annual Technical Conference and Exhibition*. Society of Petroleum Engineers.

Kuila, U., Prasad, M., Derkowski, A., & McCarty, D. K. (2012, January). Compositional controls on mudrock pore-size distribution: An example from Niobrara Formation. In *SPE Annual Technical Conference and Exhibition*. Society of Petroleum Engineers.

Kus, J., Araujo, C. V., Borrego, A. G., Flores, D., Hackley, P. C., Hámor-Vidó, M., ... & Mendonça Filho, J. G. (2017). Identification of alginite and bituminite in rocks other than coal. 2006, 2009, and 2011 round robin exercises of the ICCP Identification of Dispersed Organic Matter Working Group. *International Journal of Coal Geology*, *178*, 26-38.

Lafargue, E., Marquis, F., & Pillot, D. (1998). Rock-Eval 6 applications in hydrocarbon exploration, production, and soil contamination studies. *Revue de l'institut français du pétrole*, *53*(4), 421-437.

Lallier-Vergès, E., Bertrand, P., Tribovillard, N., & Desprairies, A. (1995). Short-term organic cyclicities from the Kimmeridge Clay Formation of Yorkshire (GB): combined accumulation and degradation of organic carbon under the control of primary production variations. In *Organic Matter Accumulation* (pp. 3-13). Springer, Berlin, Heidelberg.

Lallier-Vergès, E., Hayes, J. M., Boussafir, M., Zaback, D. A., Tribovillard, N. P., Connan, J., & Bertrand, P. (1997). Productivity-induced sulphur enrichment of hydrocarbon-rich sediments from the Kimmeridge Clay Formation. *Chemical Geology*, *134*(4), 277-288.

Largeau, C., Casadevall, E., Kadouri, A., & Metzger, P. (1984). Formation of Botryococcus-derived kerogens—Comparative study of immature torbanites and of the extent alga Botryococcus braunii. *Organic Geochemistry*, *6*, 327-332.

Lazar, O. R., Bohacs, K. M., Macquaker, J. H., Schieber, J., & Demko, T. M. (2015). Capturing Key Attributes of Fine-Grained Sedimentary Rocks In Outcrops, Cores, and Thin Sections: Nomenclature and Description Guidelines MUDSTONES: NOMENCLATURE AND DESCRIPTION GUIDELINES. *Journal of Sedimentary Research*, *85*(3), 230-246.

Legarreta, L., & Uliana, M. A. (1991). Jurassic-Cretaceous marine oscillations and geometry of back arc basin fill, Central Argentina Andes. Macdonald, D.I.M. (ed). Sedimentation, Tectonics and Eustasy-S*ea-Level Changes at Active Plate Margins*. International Association of Sedimentologists, Special Publications, 12, 429-450.

Legarreta, L., & Villar, H. J. (2011). Geological and Geochemical Keys of the Potential Shale Resources, Argentina Basins. *Search and Discovery Article*, *80196*.

Legarreta, L., & Villar, H. J. (2015). The Vaca Muerta Formation (Late Jurassic-Early Cretaceous), Neuquén Basin, Argentina: Sequences, facies and source rock characteristics: Unconventional Resources Technology Conference. In *Extended Abstracts*.

Lewan, M. D. (1993). Laboratory simulation of petroleum formation. In *Organic geochemistry* (pp. 419-442). Springer, Boston, MA.

Löhr, S. C., Baruch, E. T., Hall, P. A., & Kennedy, M. J. (2015). Is organic pore development in gas shales influenced by the primary porosity and structure of thermally immature organic matter?. *Organic Geochemistry*, *87*, 119-132.

Loucks, R. G., Reed, R. M., Ruppel, S. C., & Jarvie, D. M. (2009). Morphology, genesis, and distribution of nanometer-scale pores in siliceous mudstones of the Mississippian Barnett Shale. *Journal of sedimentary research*, *79*(12), 848-861.

Loucks, R. G., Reed, R. M., Ruppel, S. C., & Hammes, U. (2012). Spectrum of pore types and networks in mudrocks and a descriptive classification for matrix-related mudrock pores. *AAPG bulletin*, *96*(6), 1071-1098.

Magee, R. W. (1995). Evaluation of the external surface area of carbon black by nitrogen adsorption. *Rubber Chemistry and Technology*, *68*(4), 590-600.

Mastalerz, M., Schimmelmann, A., Drobniak, A., & Chen, Y. (2013). Porosity of Devonian and Mississippian New Albany Shale across a maturation gradient: Insights from organic petrology, gas adsorption, and mercury intrusion. *AAPG bulletin*, *97*(10), 1621-1643.

Milliken, K. L., Rudnicki, M., Awwiller, D. N., & Zhang, T. (2013). Organic matter–hosted pore system, Marcellus formation (Devonian), Pennsylvania. *AAPG bulletin*, *97*(2), 177-200.

Oschmann, W. (1988). Kimmeridge Clay sedimentation—a new cyclic model. *Palaeogeography, Palaeoclimatology, Palaeoecology*, *65*(3-4), 217-251.

Pan, C., Geng, A., Zhong, N., Liu, J., & Yu, L. (2009). Kerogen pyrolysis in the presence and absence of water and minerals: amounts and compositions of bitumen and liquid hydrocarbons. *Fuel*, *88*(5), 909-919.

Pan, L., Xiao, X., Tian, H., Zhou, Q., Chen, J., Li, T., & Wei, Q. (2015). A preliminary study on the characterization and controlling factors of porosity and pore structure of the Permian shales in Lower Yangtze region, Eastern China. *International Journal of Coal Geology*, *146*, 68-78.

Powell, J. H. (2010). Jurassic sedimentation in the Cleveland Basin: a review. *Proceedings of the Yorkshire Geological Society*, *58*(1), 21-72.

Ramanampisoa, L., & Disnar, J. R. (1994). Primary control of paleoproduction on organic matter preservation and accumulation in the Kimmeridge rocks of Yorkshire (UK). *Organic geochemistry*, *21*(12), 1153-1167.

Rawson, P. F., & Riley, L. A. (1982). Latest Jurassic - Early Cretaceous Events and the "Late Cimmerian Unconformity" in North Sea Area. *AAPG Bulletin*. ***66***(12), 2628-2648.

Reed, R. M., Loucks, R. G., & Ruppel, S. C. (2014). Comment on “Formation of nanoporous pyrobitumen residues during maturation of the Barnett Shale (Fort Worth Basin)” by Bernard et al.(2012). *International Journal of Coal Geology*, *127*, 111-113.

Reed, R. M. (2017). Organic-Matter Pores: New Findings from Lower-Thermal-Maturity Mudrocks. GCAGS Journal 6, 99–110.

Ross, D. J., & Bustin, R. M. (2009). The importance of shale composition and pore structure upon gas storage potential of shale gas reservoirs. *Marine and Petroleum Geology*, *26*(6), 916-927.

Schieber, J. (2010, January). Common themes in the formation and preservation of intrinsic porosity in shales and mudstones-illustrated with examples across the Phanerozoic. In *SPE Unconventional Gas Conference*. Society of Petroleum Engineers.

Sigal, R. F. (2009). A methodology for blank and conformance corrections for high pressure mercury porosimetry. *Measurement Science and Technology*, *20*(4), 045108.

Sing, K. S. (1985). Reporting physisorption data for gas/solid systems with special reference to the determination of surface area and porosity (Recommendations 1984). *Pure and applied chemistry*, *57*(4), 603-619.

Tannenbaum, E., & Kaplan, I. R. (1985). Role of minerals in the thermal alteration of organic matter—I: generation of gases and condensates under dry condition. *Geochimica et Cosmochimica Acta*, *49*(12), 2589-2604.

Tian, H., Pan, L., Xiao, X., Wilkins, R. W., Meng, Z., & Huang, B. (2013). A preliminary study on the pore characterization of Lower Silurian black shales in the Chuandong Thrust Fold Belt, southwestern China using low pressure N2 adsorption and FE-SEM methods. *Marine and Petroleum Geology*, *48*, 8-19.

Tian, H., Pan, L., Zhang, T., Xiao, X., Meng, Z., & Huang, B. (2015). Pore characterization of organic-rich lower Cambrian shales in Qiannan depression of Guizhou province, Southwestern China. *Marine and Petroleum Geology*, *62*, 28-43.

Tissot, B. P., & Welte, D. H. (1984). From kerogen to petroleum. In *Petroleum formation and occurrence* (pp. 160-198). Springer, Berlin, Heidelberg.

Uliana, M. A., Legarreta, L., Laffitte, G. A., & Villar, H. (1999, March). Estratigrafía y geoquímica de las facies generadoras de hidrocarburos en las cuencas petrolíferas de Argentina. In *4° Congreso de Exploración y Desarrollo de Hidrocarburos, Simposio, Actas* (Vol. 1, pp. 1-61).

Vergani, G., Arregui, C., Carbone, O., Leanza, H. A., Danieli, J. C., & Vallés, J. M. (2011). Sistemas petroleros y tipos de entrampamientos en la Cuenca Neuquina. In *Geologıa y Recursos Naturales de la Provincia de Neuquén: XVIII Congreso Geológico Argentino* (pp. 645-656).

Wang, Y., Zhu, Y., Chen, S., & Li, W. (2014). Characteristics of the nanoscale pore structure in Northwestern Hunan shale gas reservoirs using field emission scanning electron microscopy, high-pressure mercury intrusion, and gas adsorption. *Energy & Fuels*, *28*(2), 945-955.

Washburn, E. W. (1921). The dynamics of capillary flow. *Physical review*, *17*(3), 273.

Figures and tables

Tab.1. Main parameters from Rock Eval pyrolysis for Vaca Muerta (VMF) and Kimmeridge Clay samples (KCF). TOC: Total Organic Carbon (wt.%). S_1: free hydrocarbons (mg HC/g of rock). S_2: pyrolizable hydrocarbons (mg HC/ g of rock). T_{max}: temperature of the S_2 peak (°C). HI: Hydrogen Index (mg HC/g of TOC). OI: Oxygen Index (mg CO_2/g of TOC). RC: Residual Carbon.

Sample no.	Formation-well	Depth (m)	TOC (wt.%)	S1 (mg HC/g rock)	S2 (mg HC /g rock)	Tmax (°C)	HI (mg HC/g TOC)	OI (mg CO_2/g TOC)	RC/TOC**
Eb 3	KCF-Ebberston	69.11	8.3	0.9	52.7	425	636	18	0.47
Eb 4	KCF-Ebberston	69.14	7.1	0.2	37.2	428	528	17	0.57
Eb 8	KCF-Ebberston	69.48	6.4	0.7	39.6	429	616	20	0.49
Eb 11	KCF-Ebberston	69.9	4.2	0.3	24.6	428	586	21	0.51
Eb 19	KCF-Ebberston	69.98	10.6	0.4	61.5	428	580	15	0.52
Eb 28	KCF-Ebberston	70.01	3.2	0.1	7.9	434	249	20	0.78
Eb 30	KCF-Ebberston	70.03	5.4	0.1	18.9	432	353	18	0.71
Eb 32	KCF-Ebberston	70.05	6.6	0.2	30.5	429	462	17	0.62
Eb 34	KCF-Ebberston	70.12	12.6	0.5	80.4	425	638	18	0.48
Eb 38	KCF-Ebberston	70.25	13.4	0.9	81.3	423	607	17	0.50
Eb 40	KCF-Ebberston	70.28	15.9	0.9	97.7	424	613	19	0.49
Eb 48	KCF-Ebberston	70.65	6.0	0.1	27.3	428	456	18	0.62
		Mean	**8.3**	**0.4**	**46.6**	**427**	**527**	**18**	**0.56**
	KCF-Ebberston	**Min**	**3.2**	**0.1**	**7.9**	**423**	**249**	**15**	**0.47**
		Max	**15.9**	**0.9**	**97.7**	**434**	**638**	**21**	**0.78**
Blc 2	KCF-Marton	128.15	3.0	0.1	13.3	433	439	25	0.63
Blc 4	KCF-Marton	128.25	3.2	0.1	13.8	431	428	27	0.62
Blc 8	KCF-Marton	128.28	2.9	0.1	12.4	433	427	26	0.64
Blc 13	KCF-Marton	128.40	3.0	0.1	12.3	434	414	22	0.65
Blc 23	KCF-Marton	128.65	5.6	0.3	29.8	432	537	15	0.56
Blc 30	KCF-Marton	128.75	11.2	1.5	70.2	428	628	15	0.48
Blc 31	KCF-Marton	128.78	6.9	0.5	42.2	432	615	18	0.49
Blc 43	KCF-Marton	129.10	2.2	0.1	6.7	433	307	31	0.74
Blc 50	KCF-Marton	129.20	2.1	0.1	5.7	433	275	30	0.76
		Mean	**4.4**	**0.3**	**22.9**	**432**	**452**	**23**	**0.62**
	KCF-Marton	**Min**	**2**	**0**	**6**	**428**	**275**	**15**	**0.48**
		Max	**11**	**1**	**70**	**434**	**628**	**31**	**0.76**
93X	VMF-well	2647	2.1	0.3	0.8	/	38	19	0.95
94B	VMF-well	2668	5.0	1.2	2.2	/	43	5	0.94
95G	VMF-well	2685	3.6	0.5	0.6	/	16	15	0.97
96Z	VMF-well	2697	7.3	1.1	1.8	515*	25	5	0.96
97U	VMF-well	2710	3.9	0.5	0.9	/	23	11	0.97
98M	VMF-well	2720	5.5	0.7	1.4	/	25	6	0.97
99W	VMF-well	2734	5.4	0.8	1.3	507*	24	7	0.96
100C	VMF-well	2747	3.2	0.3	0.8	/	26	9	0.97
101E	VMF-well	2764	4.3	0.3	1.7	/	39	6	0.96
102R	VMF-well	2769	6.7	1.1	1.3	488*	19	4	0.97
103K	VMF-well	2789	9.1	1.2	1.6	500*	18	2	0.96
104P	VMF-well	2794	1.3	0.1	0.7	/	49	20	0.90
		Mean	**4.8**	**0.7**	**1.3**	**502**	**29**	**9**	**0.96**
	VMF-well	**Min**	**1.3**	**0.1**	**0.6**	**488**	**16**	**2**	**0.90**
		Max	**9.1**	**1.2**	**2.2**	**515**	**49**	**20**	**0.97**

/: unmeasurable Tmax due to a flat S2 peak. *: Tmax values which appear to be correct despite a low S2 peak. **RC/TOC: the closer this ratio is to unity, the greater the amount of residual carbon (RC) is.

1 Tab.2. Mineralogical composition obtained using X-ray diffraction analysis (in weight %) for

2 Kimmeridge Clay (Ebberston, Marton boreholes) and Vaca Muerta samples (VMF).

Sample no.	Well	Depth (m)	Quartz (wt.%)	Carbonate (wt.%)			Total carbonate (wt.%)	Gypsum (wt.%)	Albite (wt.%)	Total clay (wt.%)	Pyrite (wt.%)
				Calcite	Siderite	Dolomite					
Eb 4	Ebberston	69.14	15.9	8.5	0	0	8.5	2.0	2.5	57.6	6.4
Eb 19	Ebberston	69.98	8.7	17.6	0	0	17.6	0.8	3.0	53.6	5.7
Eb 28	Ebberston	70.01	19.8	22.4	0	0	22.4	0	6.1	46.6	2.0
Eb 40	Ebberston	70.28	7.8	13.8	0	0	13.8	1.4	1.5	54.6	5.0
Eb 48	Ebberston	70.65	15.8	19.5	0	0	19.5	1.0	1.9	54.8	1.0
	Min		7.8	**8.5**	**0**	**0**	**8.5**	**0**	**1.5**	**46.6**	**1.0**
	Max		**19.8**	**22.4**	**0**	**0**	**22.4**	**2.0**	**6.1**	**57.6**	**6.4**
	Mean		**13.6**	**16.4**	**0**	**0**	**16.4**	**1.0**	**3.0**	**53.4**	**4.02**
Blc 2	Marton	128.15	19.7	16.3	4.6	0	20.9	1.1	2.6	52.5	0.2
Blc 13	Marton	128.40	21.5	19.7	4.4	0	24.1	1.7	0	49.0	0.7
Blc 30	Marton	128.75	14.3	15.0	0	0	15.0	0.8	6.2	46.0	6.4
Blc 31	Marton	128.78	14.3	17.0	1.0	0	18.0	0.6	2.7	54.1	3.5
Blc 50	Marton	129.20	12.4	6.5	13.7	0	20.2	1.1	3.8	59.1	1.3
	Min		**12.4**	**6.5**	**0**	**0**	**15.0**	**0.8**	**0**	**46.0**	**0.2**
	Max		**21.5**	**19.7**	**13.7**	**0**	**24.1**	**1.7**	**6.2**	**59.1**	**6.4**
	Mean		**16.4**	**14.9**	**4.7**	**0**	**19.6**	**1.1**	**3.1**	**52.1**	**2.42**
94B	VMF	2668	31.5	10.0	0.3	0.5	10.8	0	21.1	30.0	1.6
96Z	VMF	2697	15.6	28.8	0.2	0	29.0	0	23.6	22.2	2.4
98M	VMF	2720	33.7	14.2	0.1	0	14.3	0	22.8	22.1	1.6
100C	VMF	2747	39.1	8.1	0	0	8.1	0	26.4	21.7	1.5
102R	VMF	2769	27.7	12.8	0.2	0	13.0	0	27.9	23.3	1.4
103K	VMF	2789	22.1	6.5	0.1	0	6.6	0	24.6	36.1	1.6
	Min		**15.6**	**6.5**	**0**	**0**	**6.6**	**0**	**21.1**	**21.7**	**1.4**
	Max		**39.1**	**28.8**	**0.3**	**0.5**	**29.0**	**0**	**27.9**	**36.1**	**2.4**
	Mean		**28.3**	**13.4**	**0.1**	**0.1**	**13.6**	**0**	**24.4**	**25.9**	**1.7**

3

Tab.3. Porosity measurements obtained from mercury intrusion porosimetry including raw data and corrected data from surface roughness for Vaca Muerta (VMF) and Kimmeridge Clay mudstones (Marton, Ebberston boreholes). Contribution of macropores corresponds to the contribution to the total pore volume of macropores ranging between 50 nm - 6µm in diameter. PV: pore volume. TP: Total porosity.

		Raw data				Corrected data			
Sample no.	**Well**	**PV (cm^3/100g)**	**TP (%)**	**skeletal density (g/cm^3)**	**bulk density (g/cm^3)**	**PV (cm^3/100g)**	**TP (%)**	**Cumulated PV at 50 nm (cm^3/100g)**	**Contribution of macropores (%)**
Eb 4	Ebberston	9.93	19.58	2.45	1.97	3.06	6.04	0.55	17.99
Eb 19	Ebberston	10.51	18.60	2.17	1.77	3.10	5.48	0.40	12.97
Eb 28	Ebberston	10.10	19.76	2.44	1.96	5.06	9.91	0.64	12.59
Eb 40	Ebberston	12.16	19.01	2.06	1.56	3.00	4.70	0.52	17.24
Eb 48	Ebberston	13.05	23.40	2.34	1.79	5.57	9.98	0.97	17.37
	Mean	**11.15**	**20.07**	**2.29**	**1.81**	**3.96**	**7.22**	**0.61**	**15.63**
Blc 2	Marton	9.72	19.49	2.49	2.01	2.61	5.23	0.28	10.80
Blc 13	Marton	8.35	16.91	2.44	2.02	2.39	4.85	0.27	11.12
Blc 30	Marton	10.59	18.84	2.19	1.78	1.89	3.37	0.43	22.84
Blc 31	Marton	8.33	15.69	2.24	1.88	2.14	4.03	0.49	22.75
Blc 50	Marton	10.13	20.13	2.49	1.99	3.07	6.09	0.33	10.63
	Mean	**9.42**	**18.21**	**2.37**	**1.94**	**2.42**	**4.71**	**0.36**	**15.63**
93X	VMF	16.31	28.68	2.47	1.76	1.63	2.87	0.15	8.91
96Z	VMF	16.59	28.49	2.40	1.72	0.36	0.61	0.03	8.26
98M	VMF	15.96	28.10	2.45	1.76	1.31	2.29	0.09	6.69
103K	VMF	9.76	16.69	2.33	1.70	0.35	0.59	0.02	7.00
	Mean	**14.65**	**25.49**	**2.41**	**1.73**	**0.91**	**1.59**	**0.07**	**7.71**

Tab.4. Porosity measurements obtained by nitrogen adsorption analysis including BET specific surface areas (S_{BET}) and total pore volumes (P_{vol}) for Vaca Muerta (VMF) and Kimmeridge Clay samples (Marton, Ebberston boreholes). Comparison of the two models frequently used in the community for the T-plot methods: the universal t-curve based on the Harkins-Jura model and the Carbon-black model specific for carbon-rich materials. V_{micro}: micropore volume. S_{micro}: micropore specific surface area. Sext: external specific surface area ($S_{micro} = S_{BET}$ - Sext). Vmicro contribution (%) is the contribution of the micropore volume to the total pore volume (%).

					T-plot methods								
					Harkins-Jura model				**Carbon black model**				
Sample no.	**Well**	**TOC (%)**	**S_{BET} (m^2/g)**	**P_{vol} ($cm^3/100g$)**	**S_{micro} (m^2/g)**	**S_{ext} (m^2/g)**	**V_{micro} ($cm^3/100g$)**	**V_{ext} ($cm^3/100g$)**	**S_{micro} (m^2/g)**	**S_{ext} (m^2/g)**	**V_{micro} ($cm^3/100g$)**	**V_{ext} ($cm^3/100g$)**	**V_{micro} contribution (%)**
93X	VMF	2.1	13.52	2.24	9.72	3.80	0.50	1.74	10.29	3.23	0.50	1.74	22.4
100C	VMF	3.2	17.54	2.76	15.99	1.54	0.80	1.96	16.06	1.48	0.80	1.96	29.0
94B	VMF	5.0	22.64	3.51	11.46	11.18	0.60	2.91	9.18	13.46	0.40	3.11	11.4
98M	VMF	5.5	21.07	3.57	7.39	13.68	0.30	3.27	7.48	13.59	0.30	3.27	8.4
102R	VMF	6.7	23.36	3.54	16.03	7.33	0.80	2.74	15.43	7.93	0.80	2.74	22.6
96Z	VMF	7.3	19.37	2.68	12.52	6.84	0.60	2.08	12.16	7.20	0.60	2.08	22.4
103K	VMF	9.1	29.92	3.54	23.43	6.49	1.10	2.44	21.01	8.92	1.10	2.44	31.1
	Mean	**5.6**	**21.1**	**3.1**	**13.8**	**7.3**	**0.7**	**2.4**	**13.1**	**8.0**	**0.6**	**2.5**	**21.0**
Eb 4	Ebberston	7.1	15.53	4.42	4.85	10.68	0.10	4.32	4.79	10.75	0.10	4.32	2.3
Eb 19	Ebberston	10.6	12.06	3.63	7.42	4.65	0.40	3.23	7.22	4.85	0.40	3.23	11.0
Eb 28	Ebberston	3.2	33.96	5.41	9.28	24.68	0.50	4.91	9.86	24.09	0.50	4.91	9.2
Eb 38	Ebberston	14.4	10.32	2.82	1.61	8.70	0.10	2.72	1.36	8.95	0.10	2.72	3.5
Eb 40	Ebberston	15.9	9.59	3.17	1.29	8.30	0.10	3.07	1.12	8.47	0.10	3.07	3.2
Eb 48	Ebberston	6.0	20.01	5.62	0.73	19.28	0.00	5.62	0.57	19.44	0.00	5.62	0.0
	Mean	**9.5**	**16.9**	**4.2**	**4.2**	**12.7**	**0.2**	**4.0**	**4.2**	**12.8**	**0.2**	**4.0**	**4.9**
Blc 2	Marton	3.0	19.93	3.63	6.97	12.96	0.40	3.23	7.75	12.18	0.40	3.23	11.0
Blc 13	Marton	3.0	22.29	4.33	1.74	20.55	0.10	4.23	1.80	20.50	0.10	4.23	2.3
Blc 23	Marton	5.6	17.53	3.73	2.26	15.27	0.10	3.63	1.60	15.92	0.10	3.63	2.7
Blc 30	Marton	11.2	5.80	1.97	5.00	0.80	0.30	1.67	5.01	0.78	0.30	1.67	15.2
Blc 31	Marton	6.9	8.87	3.01	5.72	3.14	0.30	2.71	5.66	3.21	0.30	2.71	10.0
Blc 50	Marton	2.1	28.56	4.57	7.38	21.18	0.40	4.17	9.25	19.31	0.50	4.07	10.9
	Mean	**5.3**	**17.2**	**3.5**	**4.8**	**12.3**	**0.3**	**3.3**	**5.2**	**12.0**	**0.3**	**3.3**	**8.7**

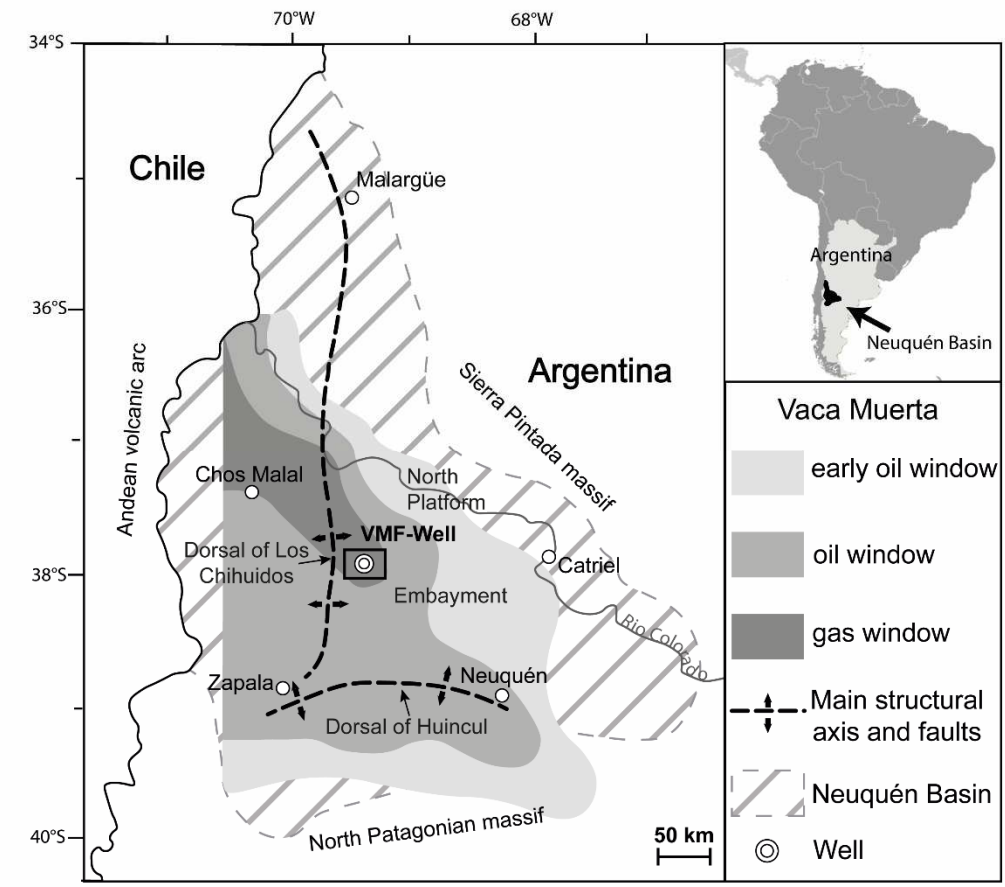

1

2 Fig.1. Location of the Vaca Muerta Formation and the studied area (VMF-Well) in the Neuquén

3 Basin, central-west Argentina (from Legarreta and Villar, 2011).

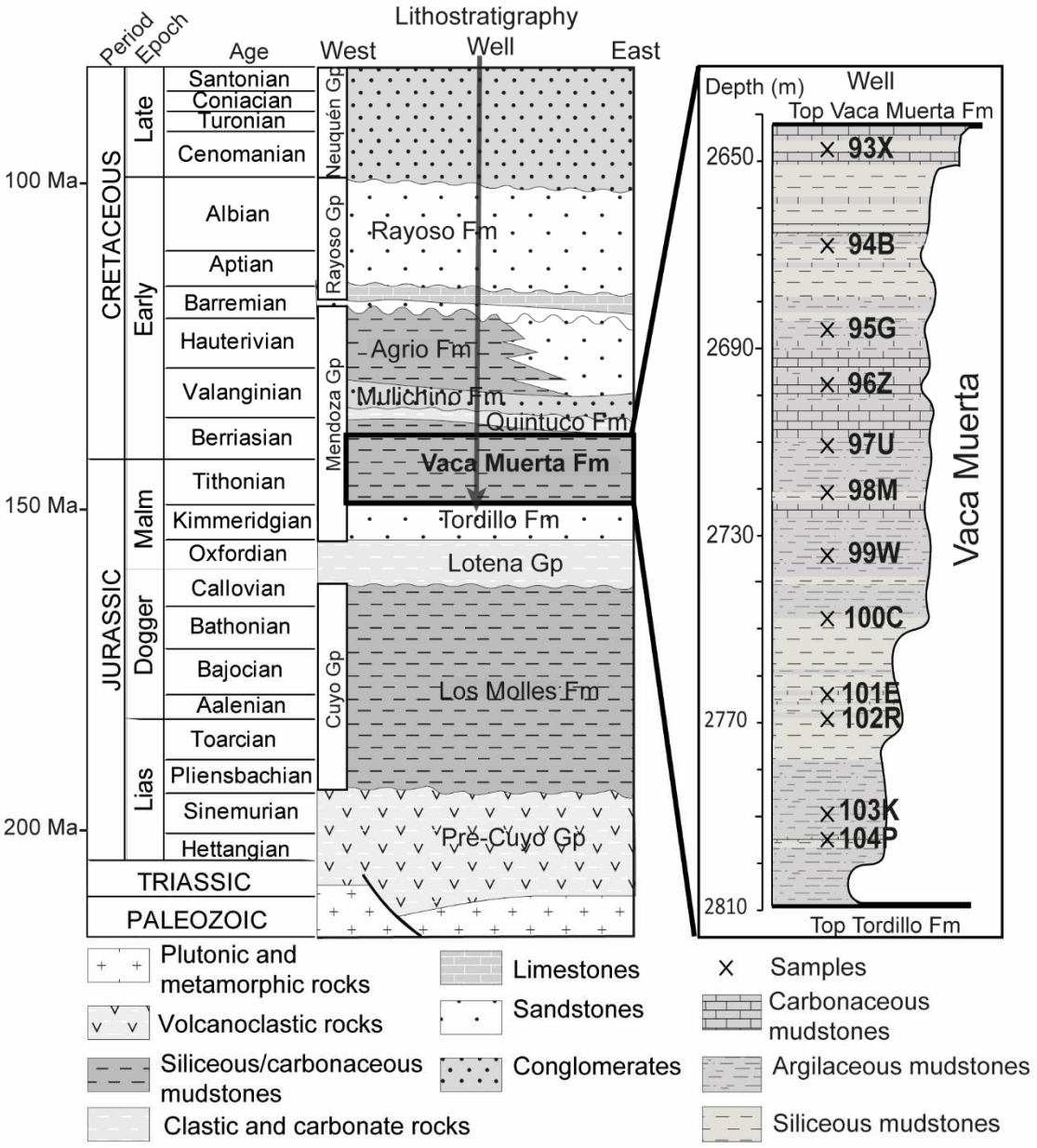

Fig.2. Chronostratigraphy of the Neuquén Basin in the studied area and distribution of samples in the investigated well. Lithostratigraphy after Howell et al. (2005) and Vergani et al. (2011).

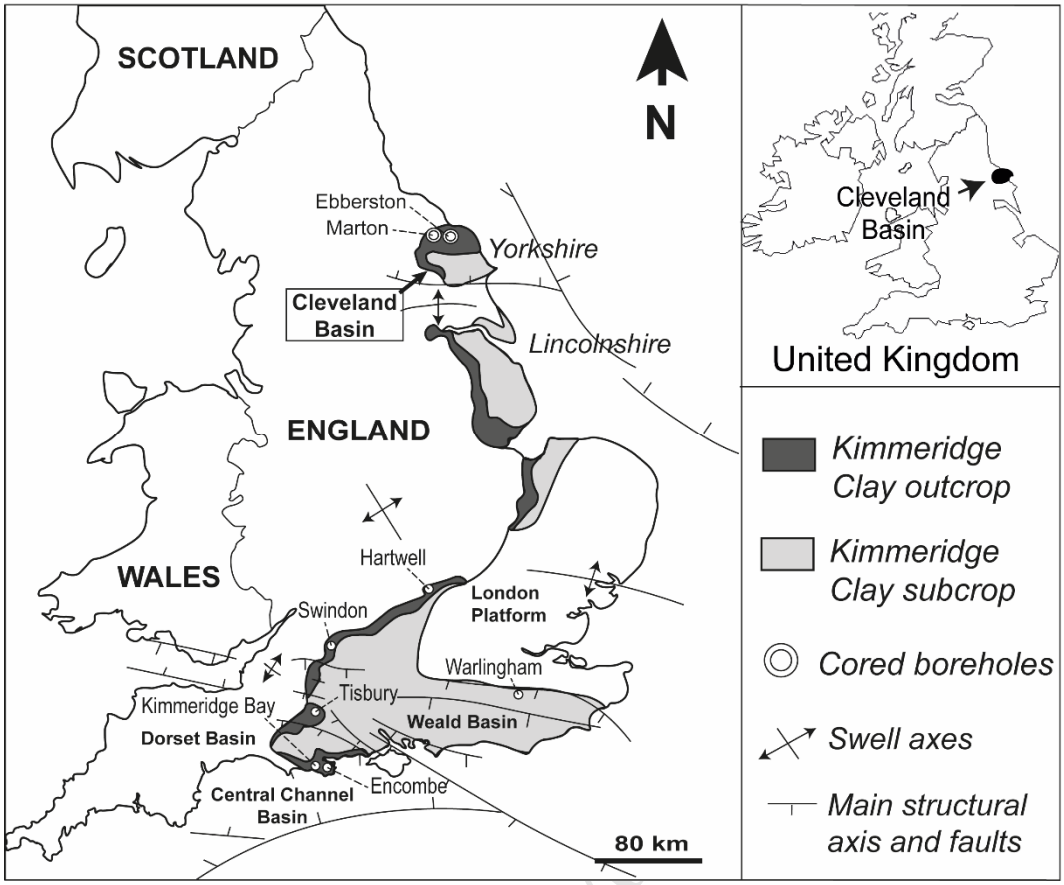

1 Fig.3. Location of the Kimmeridge Clay formation outcrops, Marton and Ebberston Holes in the

2 Cleveland Basin (Northeast of England) (from Ramanampisoa and Disnar, 1994; Herbin et al., 1991).

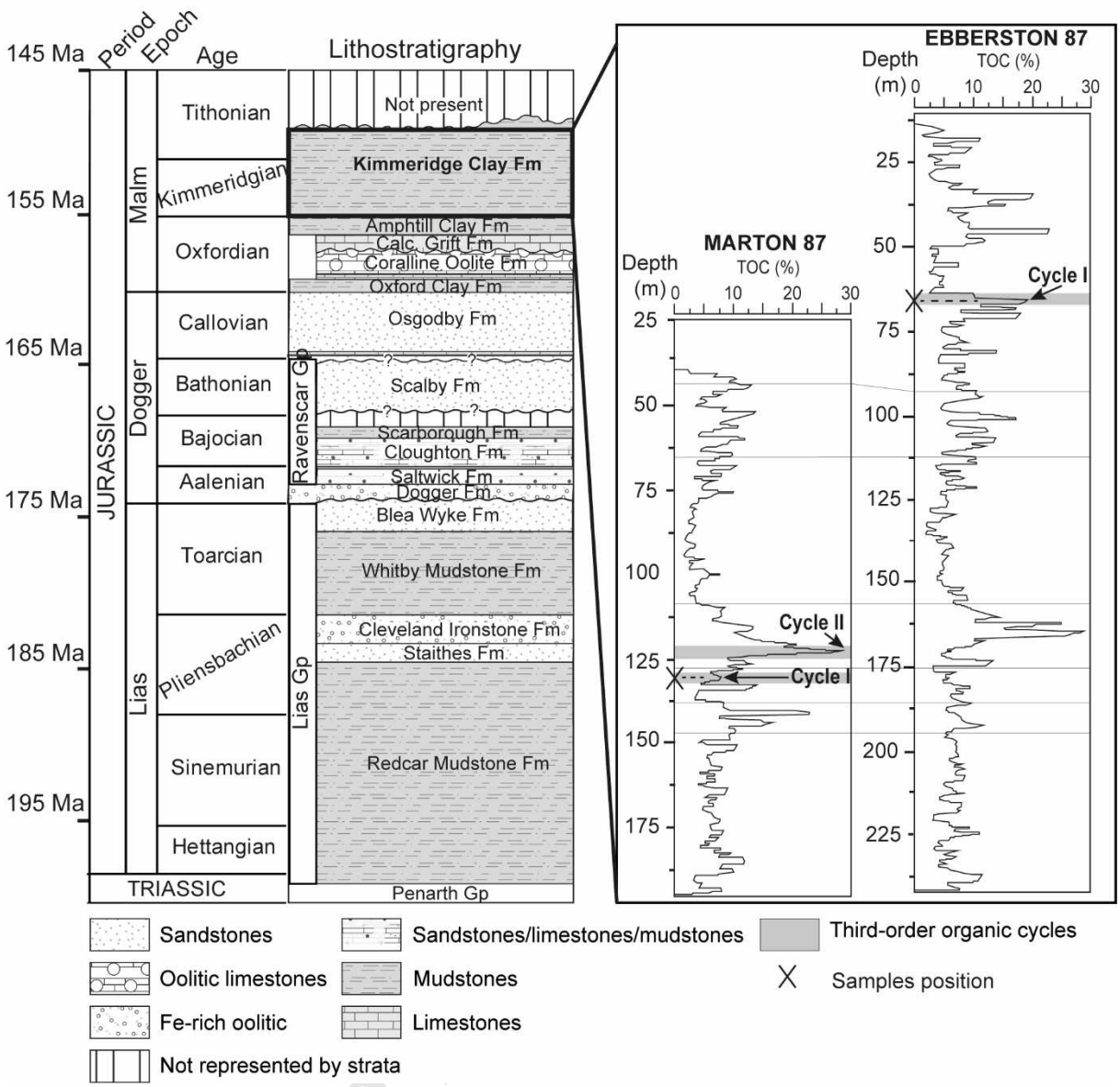

Fig.4. Simplified stratigraphic column of the Cleveland Basin (Northeast England, from Powell, 2010) and total organic carbon distribution with depth in Ebberston and Marton boreholes with studied short-term organic cycles and sample locations (from Herbin et al., 1991).

1

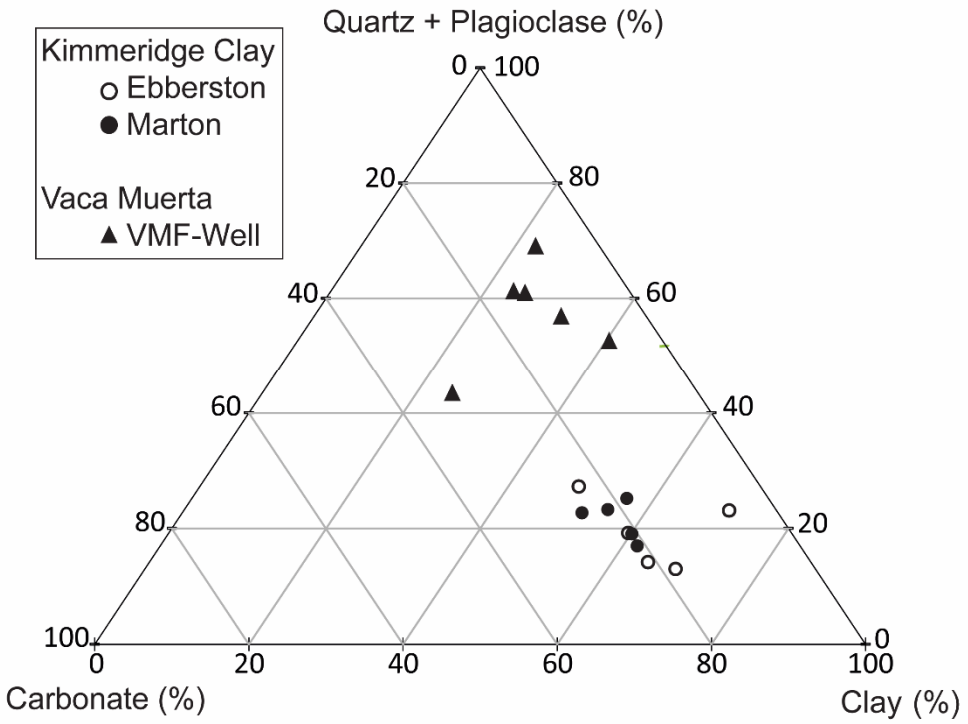

2 Fig.5. Mineralogical ternary diagram based on the normalized data from Tab.1 (in weight %).

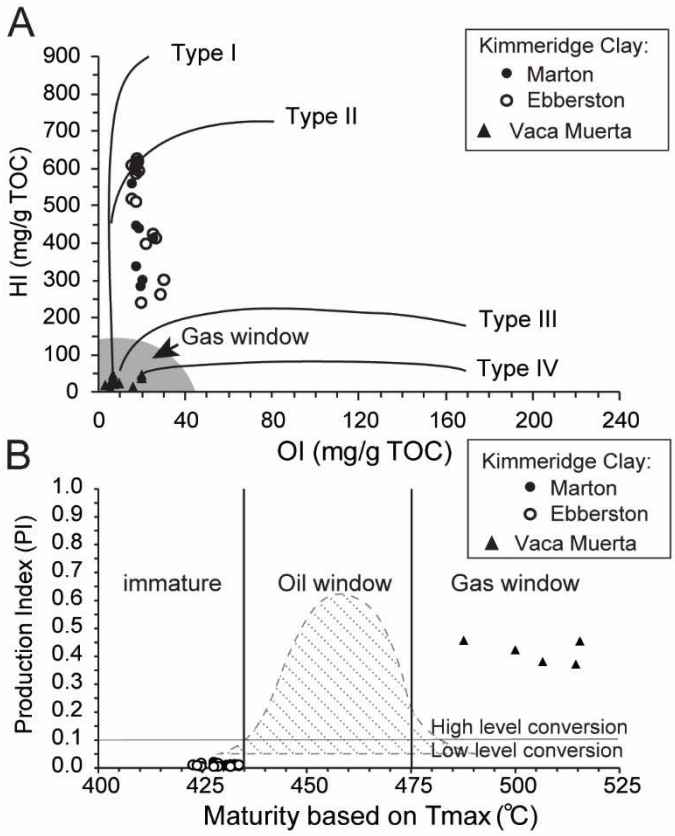

1 Fig.6. A) Pseudo-Van Krevelen diagram of Vaca Muerta and Kimmeridge Clay samples. B)

2 Production index as a function of T_{max} (data from Tab.2).

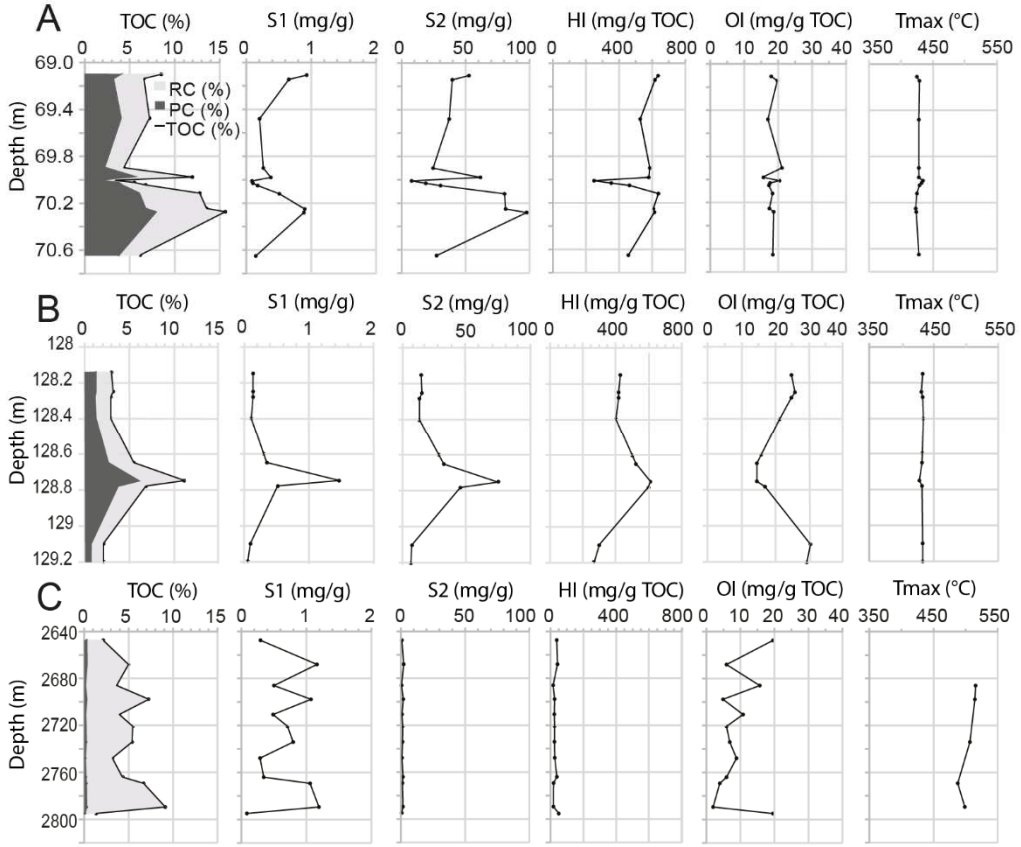

1 Fig.7. Evolution of the main petrographic parameters with depth in Ebberston (A), Marton (B)
2 (Kimmeridge Clay formation) and in the Vaca Muerta formation (C) (data from Tab.2). RC: Residual
3 Carbon. PC: pyrolizable carbon (in weight %).

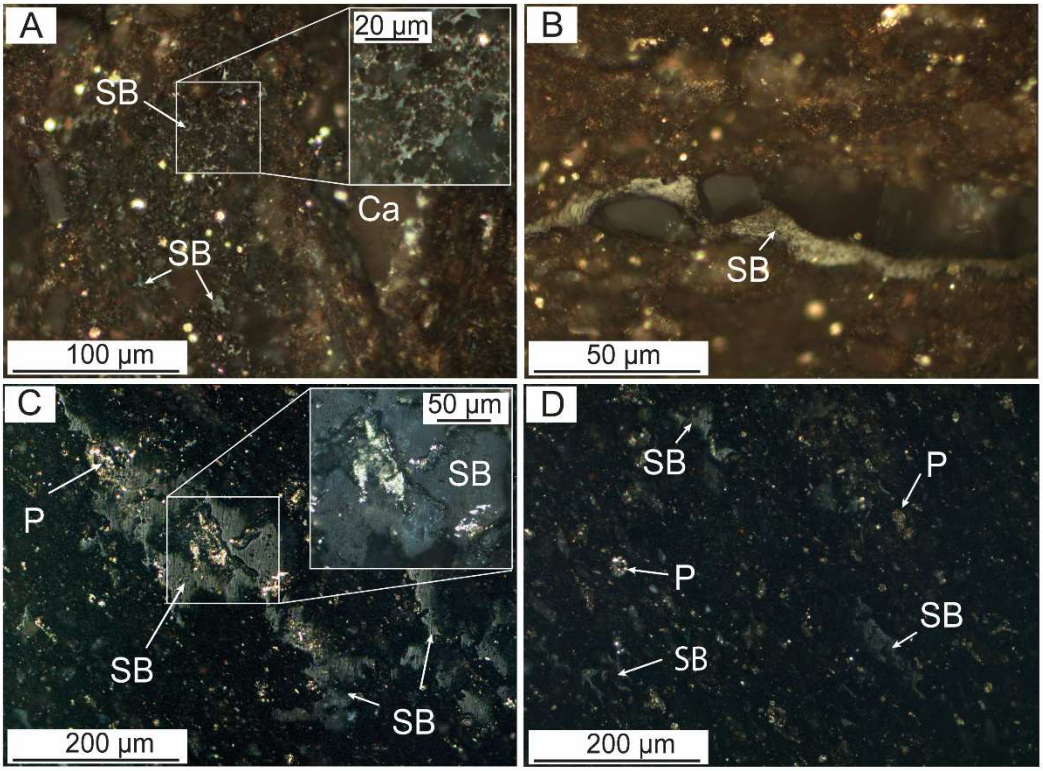

Fig.8. Incident white light photomicrographs (oil immersion) of thermally-mature (~1.65%) organic-rich Vaca Muerta mudstones (TOC = 5.0 wt.%). A) Vaca Muerta sample showing solid bitumen (SB) network. Insert in A shows solid bitumen embayed against small euhedral crystals of carbonates. B) Photomicrographs showing a solid bitumen streak (grey-white). C-D) Solid bitumen accumulations with a granular/pitted surface texture. P: pyrite. Ca: carbonate.

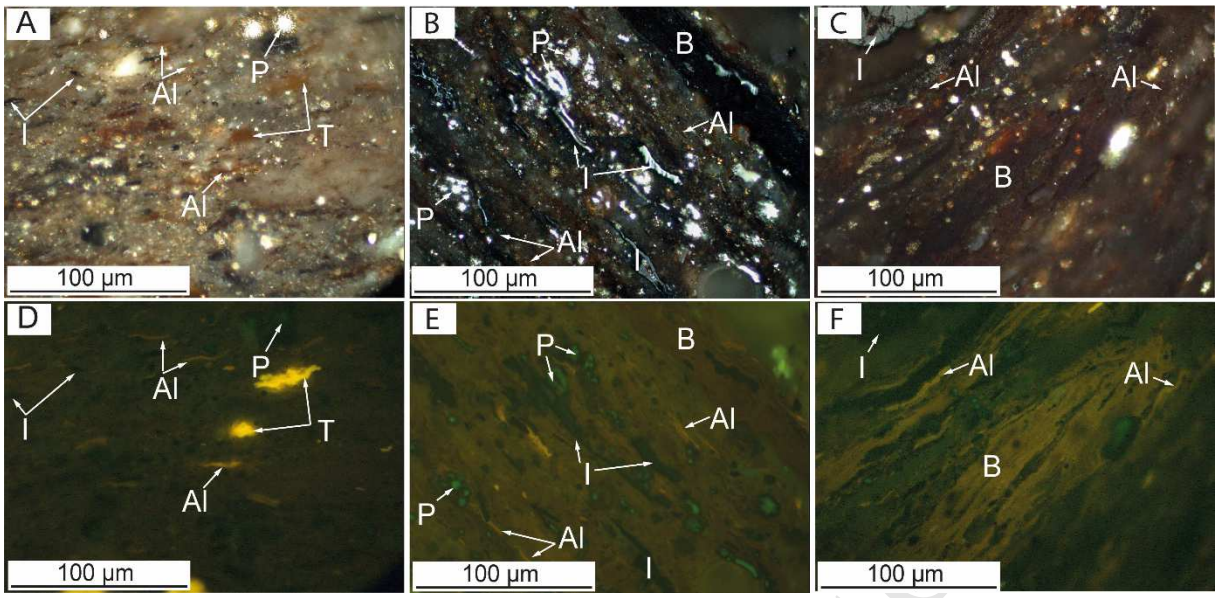

Fig.9. Incident white light (A-C) photomicrographs (oil immersion) of organic-rich Kimmeridge clay mudstones (A, TOC= 5.6 wt.%; B =10.9 wt.%; C, TOC =15.9 wt.%). D-F) Same field as A, B and C under UV-fluorescence light. Al: lamellar alginite macerals. T: *Tasmanite* algal body. B: elongated bodies of dark/brown amorphous organic matter identified as 'bituminite' macerals. I: inertinite fragments. P: pyrite framboids.

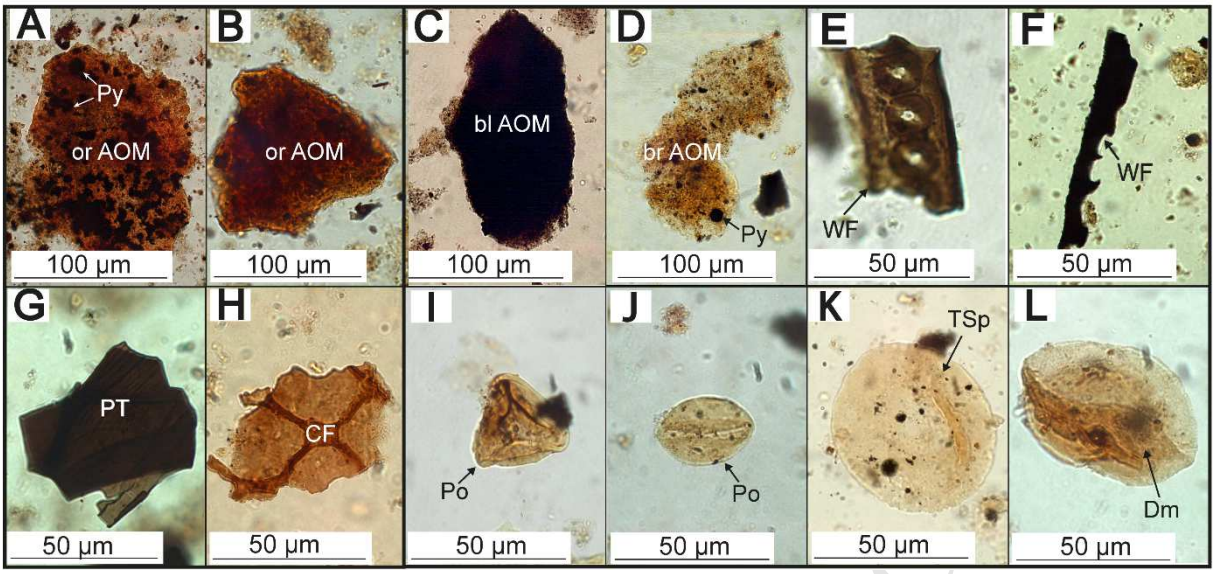

Fig.10. Different types of amorphous organic matter (A-D) and isolated structured organic matter (E-L) observed in Kimmeridge Clay samples by optical microscopy (transmitted light, oil immersion). A, B): orange amorphous organic matter (or AOM) with black pyritic inclusions (Py). C: black amorphous organic matter (bl AOM). D: brown amorphous organic matter with pyrite and oxidized debris inclusions. E: woody oxidized fragment (WF). F: opaque oxidized debris from plant tissue (WF). G: gelified membranes of plant tissue (PT). H: cuticular fragments (CF). I and J: pollen grains (Po). K: well preserved *Tasmanite*-like megaspore (Tsp). L: degraded megaspore (Dm).

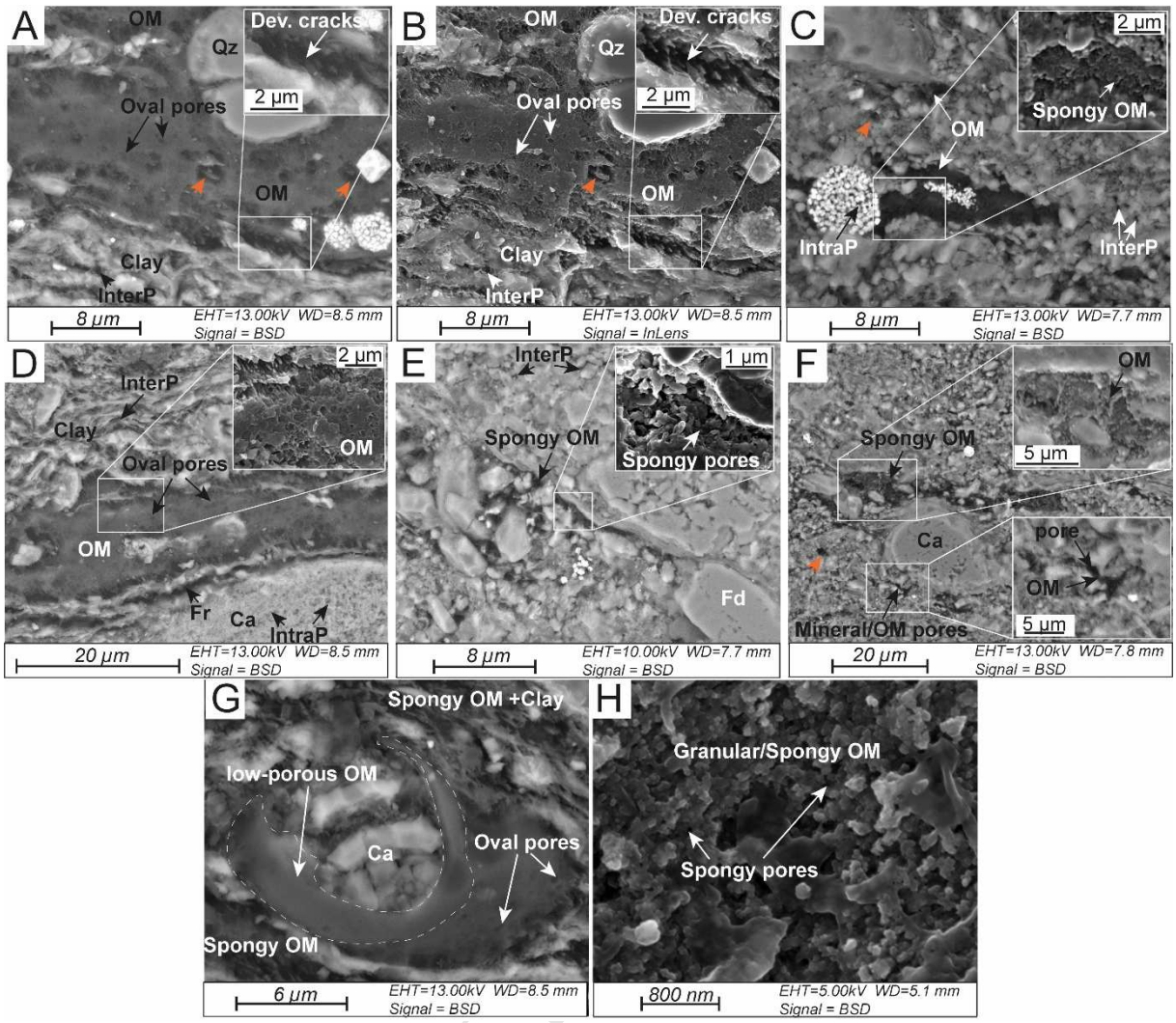

Fig.11. Scanning electron microscope images of broad ion beam milled thin sections of thermally-mature (Ro ≈1.65%) organic-rich Vaca Muerta samples (A-B, TOC=6.7 wt.%; E-H, TOC=5.0 wt.%). A, B, D) Backscattered electron (BSE) and secondary electron (SE) images showing a continuous spongy organic matter(OM)-hosted pore network with abundant oval pores. Insert in B shows the presence of some devolatilization cracks (Dev.cracks). C, E-F) BSE images showing spongy/ granular organic matter accumulations embayed in the mineral matrix. H and inserts in C-E show SE images of spongy subangular OM-hosted pores. Insert in F shows BSE images of pores located between mineral and residual OM interpreted as mineral/OM pores. G) BSE image showing a relatively low-porous organic matter area. Ca: calcite. Qz: quartz. InterP: interparticle pores. IntraP: intraparticle pores. Fr: microfracture. Some of the large macropores (orange arrows) and the microfractures observed in these samples are interpreted as artefacts due to sample grinding and polishing.

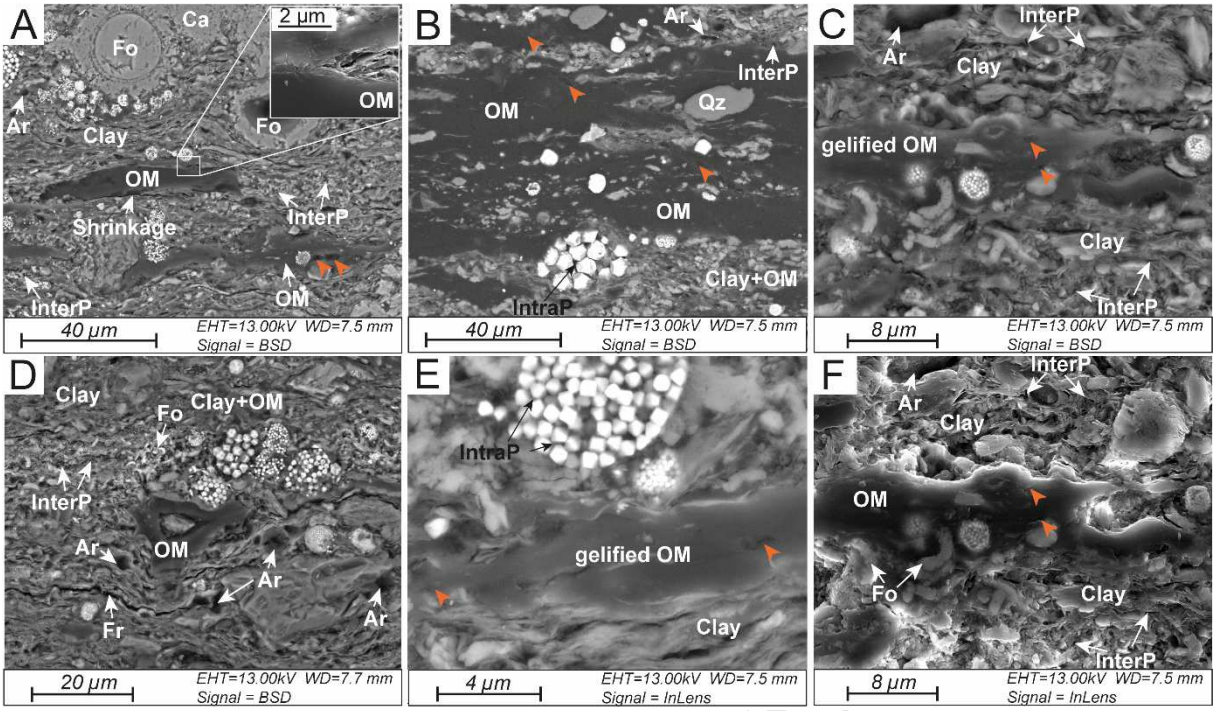

Fig.12. Scanning electron microscope images of broad ion beam milled thin sections of low-mature (Ro ≈0.5%) organic-rich Kimmeridge Clay samples (A: TOC=15.9 wt.%; B: TOC=11.2 wt.%; C-F: TOC=5.6 wt.%). A-E) BSE images showing a gelified non-porous organic matter (OM). F and insert in A show SE images of non-porous and homogeneous OM. Fr: microfracture. Ca : carbonate. Qz : quartz. InterP: interparticle pores. IntraP: intraparticle pores. Fo: microfossil debris. Rare intraparticle pores are present in OM (orange arrows). Some of the large macropores (Ar) and the microfractures (Fr) observed in these samples are interpreted as artefacts due to sample grinding and polishing.

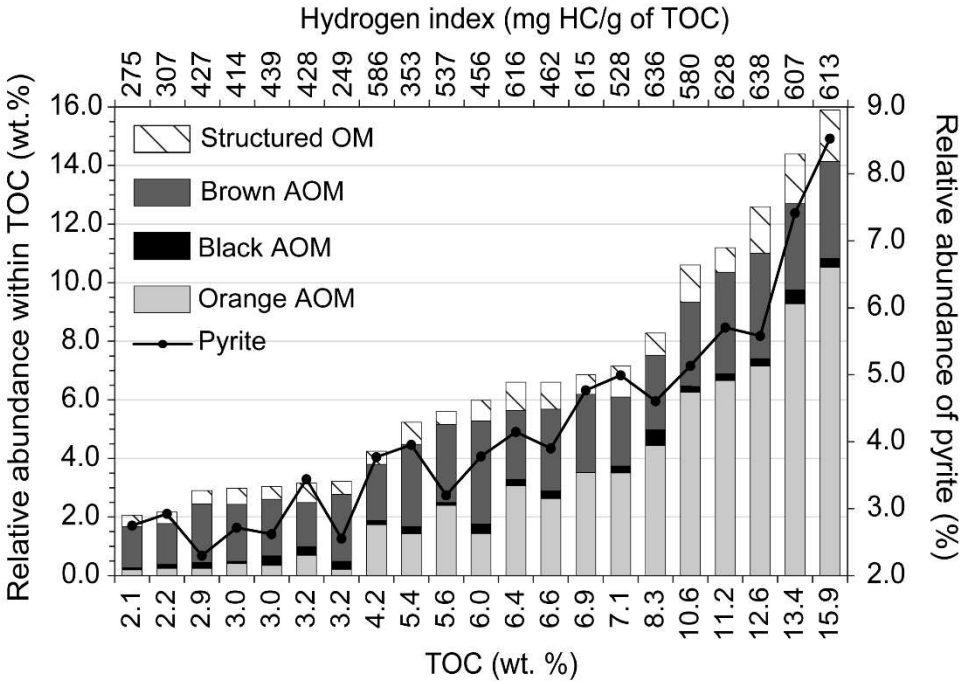

1 Fig.13. Palynofacies composition versus TOC contents and hydrogen index of Kimmeridge Clay
2 samples (including Marton and Ebberston samples). AOM: amorphous organic matter. Structured
3 OM: structured organic matter composed of various phytoclasts including woody fragments, cuticular
4 fragments and other plant tissues, pollen grains, spores and preserved phytoplankton.

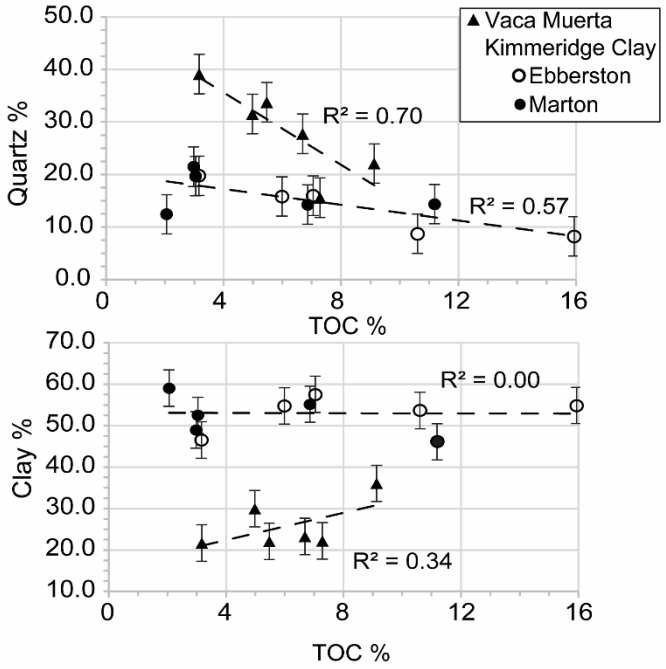

1 Fig.14. Relationships between silica, clay minerals and TOC contents in Kimmeridge Clay (Marton

2 and Ebberston holes) and Vaca Muerta samples (in weight %).

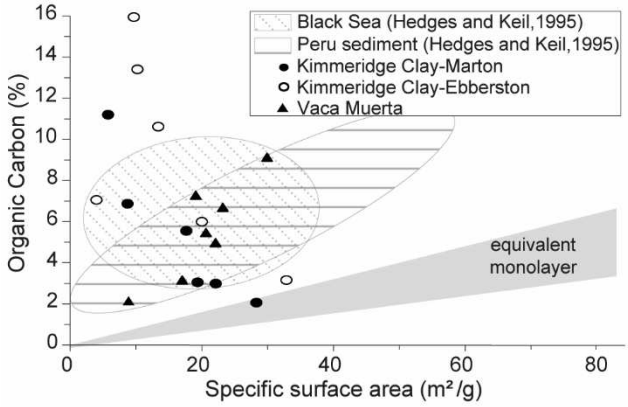

1 Fig.15: Organic carbon content as a function of specific surface area of Kimmeridge Clay and Vaca

2 Muerta samples. Comparison with the monolayer equivalent model from Hedges and Keil, (1995).

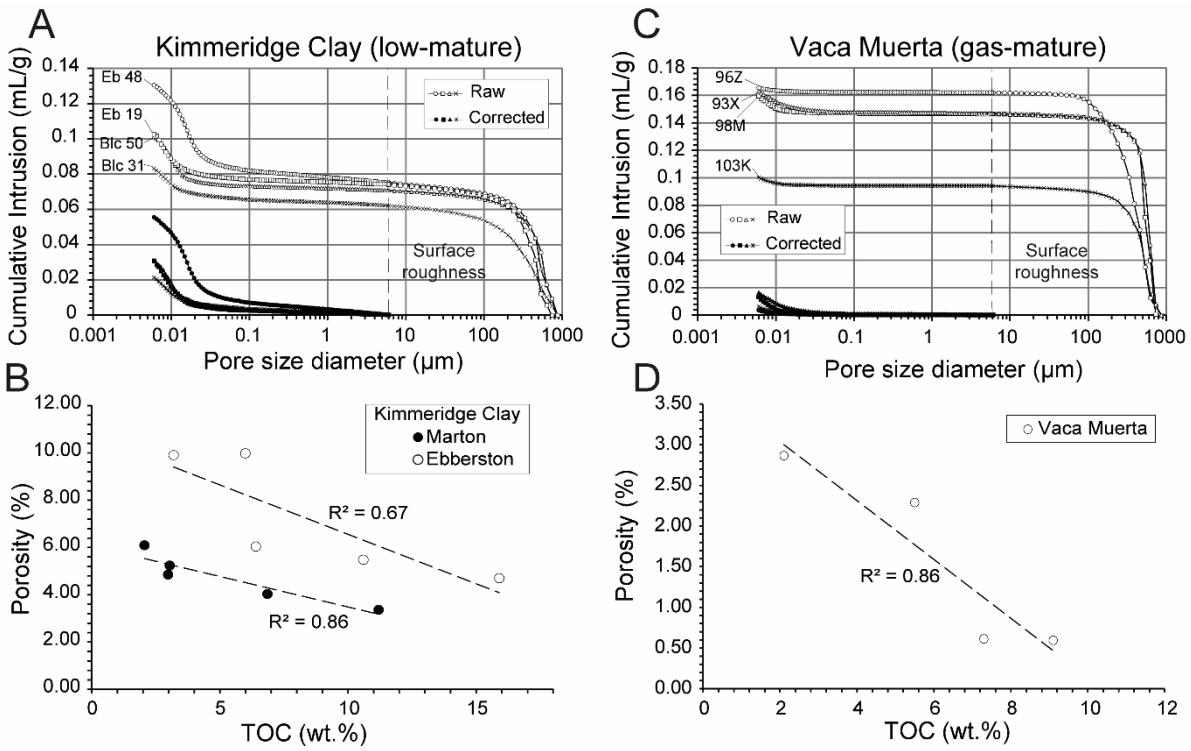

Fig.16. A, C) Examples of cumulative intrusion curves derived from mercury intrusion porosimetry as a function of pore size diameter before and after correction of conformance errors for Kimmeridge Clay and Vaca Muerta samples. B, D) Evolution of porosity as a function of TOC after correction.

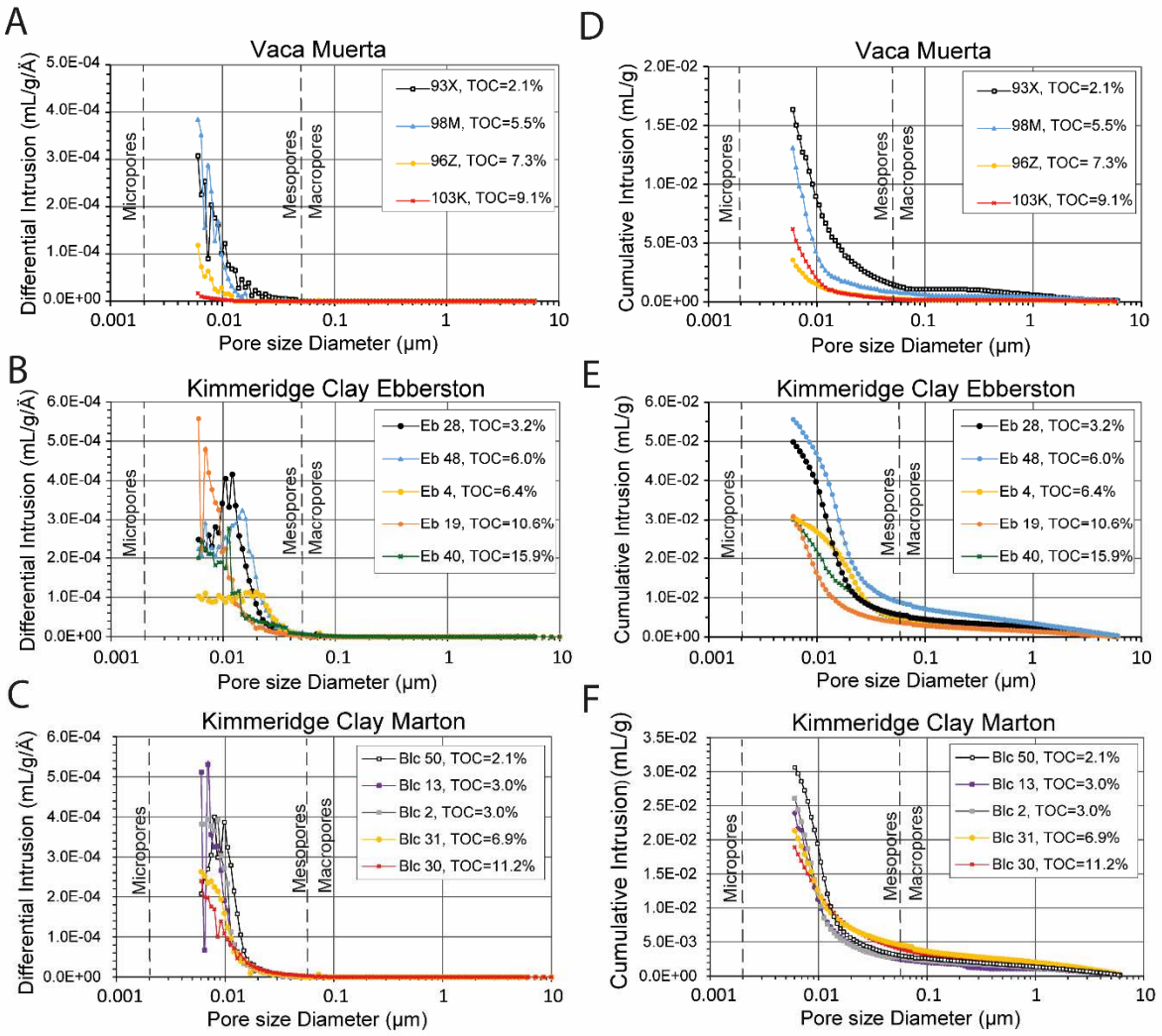

Fig.17. Pore size distributions and cumulated pore volumes (after corrections) derived from mercury intrusion porosimetry measurements as a function of TOC (in weight %) for Vaca Muerta and Kimmeridge Clay rocks.

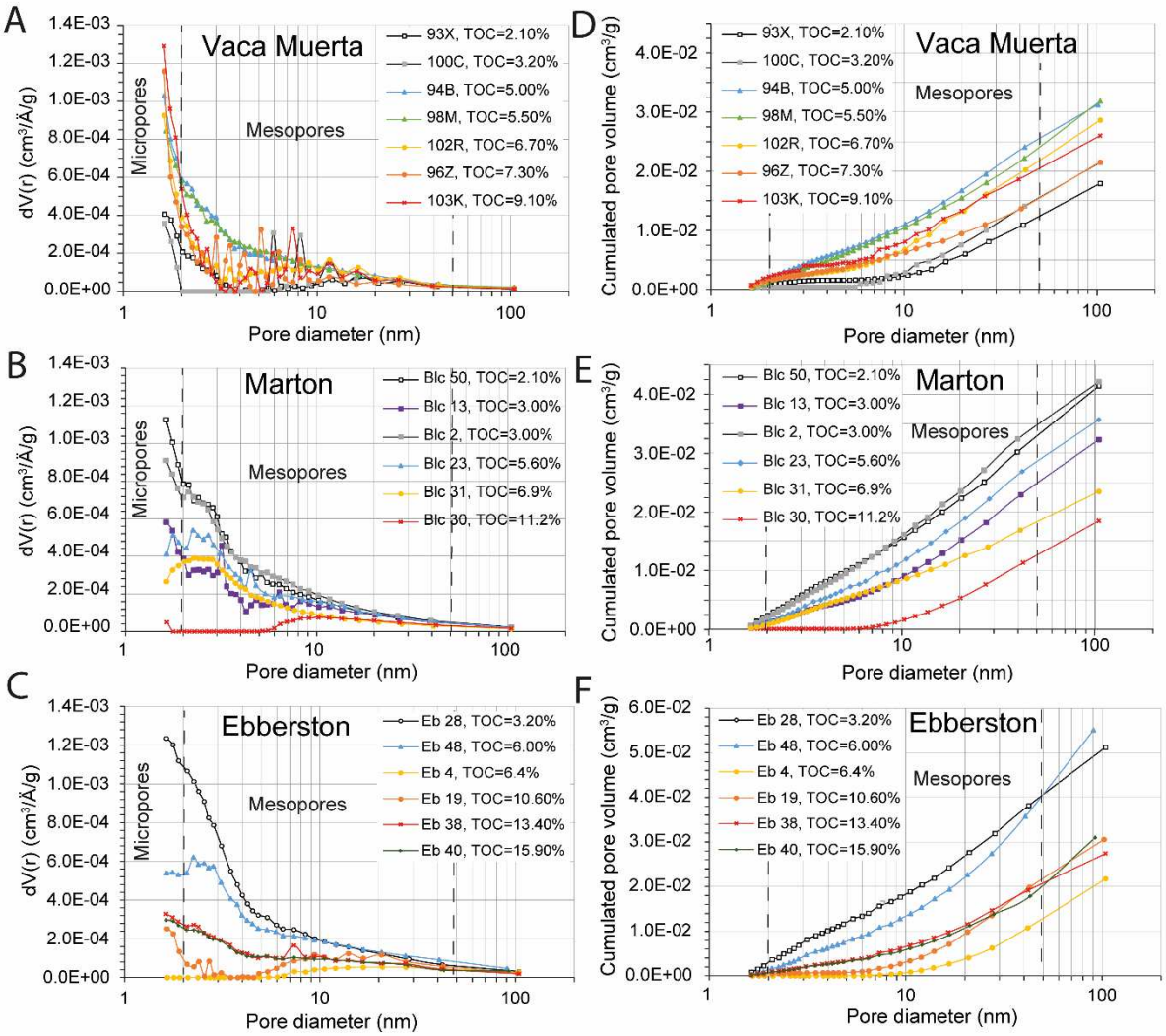

1 Fig.18. Pore size distributions and cumulated pore volumes derived from the nitrogen adsorption
2 branch for the isotherms of Kimmeridge Clay (Marton, Ebberston) and Vaca Muerta mudstones (BJH
3 model) as a function of TOC (in weight %).

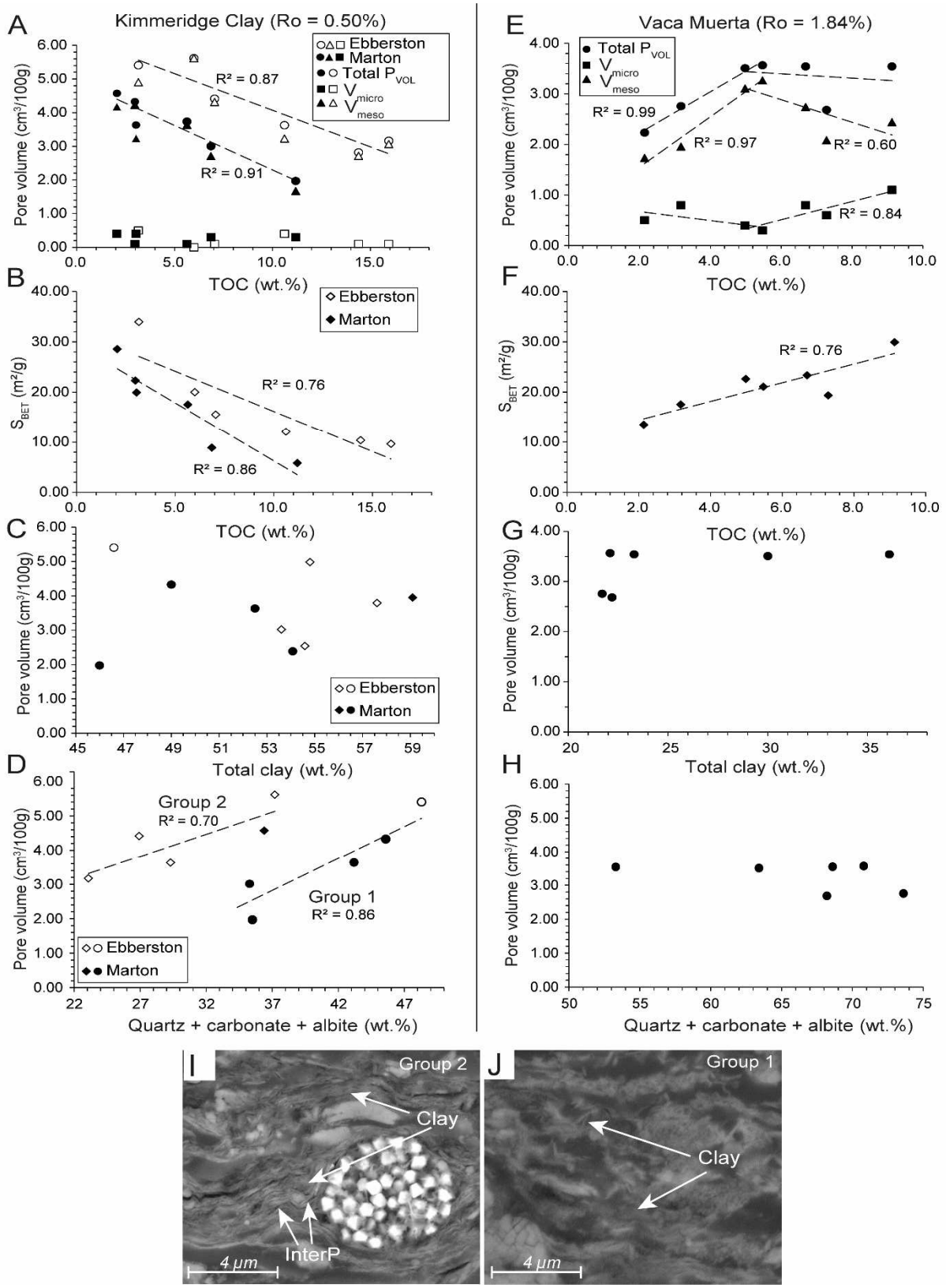

1 Fig.19. A-H) Pore volumes and specific surface areas from nitrogen adsorption measurements as a
2 function of TOC, clay, quartz, carbonate and albite contents for Vaca Muerta and Kimmeridge Clay
3 (Marton, Ebberston) mudstones. Micropore (V_{micro}) and mesopore (V_{meso}) volumes were obtained from

the T-plot method using the Carbon black model. C-D) The dots represent samples with relatively low clay mineral contents (group 1) and the diamonds stand for samples with relatively high clay mineral content (group 2). I-J) SEM images of broad ion beam milled thin sections of low-mature Kimmeridge Clay samples showing differences in the texture of clay minerals between the group 1 (J) and 2 (I). InterP: interparticle pores.

Highlights

- Shale pore networks vary significantly with thermal maturity.
- The porosity of immature shales is dominated by mineral interparticle pores.
- The porosity of gas-mature rocks is dominated by OM-hosted pores.
- A decrease in pore size with increasing TOC is observed in gas-mature samples.
- The higher oil-prone quality of high-TOC samples can influence OM-pores genesis.